

2D semiconductor device simulations by WENO-Boltzmann schemes: efficiency, boundary conditions and comparison to Monte Carlo methods

JOSÉ A. CARRILLO

ICREA - Department de Matemàtiques, Universitat Autònoma de Barcelona,

E-08193 - Bellaterra - Spain

carrillo@mat.uab.es

IRENE M. GAMBA

Department of Mathematics and ICES, University of Texas at Austin, Austin, TX 78712,

USA

gamba@math.utexas.edu

ARMANDO MAJORANA

Dipartimento di Matematica e Informatica, Università di Catania, Catania, Italy

majorana@dmi.unict.it

CHI-WANG SHU

Division of Applied Mathematics, Brown University, Providence, RI 02912, USA

shu@dam.brown.edu

Abstract

We develop and demonstrate the capability of a high order accurate finite difference weighted essentially non-oscillatory (WENO) solver for the direct numerical simulation of transients for a two space dimensional Boltzmann transport equation (BTE) coupled with the Poisson equation modeling semiconductor devices such as the MESFET and MOSFET. We compare the simulation results with those obtained by a direct simulation Monte Carlo (DSMC) solver for the same geometry. The main goal of this work is to benchmark and clarify the implementation of boundary conditions for both, deterministic and Monte Carlo numerical schemes modeling these devices, to explain the boundary singularities for both the electric field and mean velocities associated to the solution of the transport equation, and to demonstrate the overall excellent behavior of the deterministic code through the good agreement between the Monte Carlo results and the coarse grid results of the deterministic WENO-BTE scheme.

Keywords: Weighted Essentially Non-Oscillatory (WENO) schemes; Boltzmann Transport Equation (BTE); semiconductor device simulation; MESFET; MOSFET; Direct Simulation Monte Carlo (DSMC).

Report Documentation Page

Form Approved
OMB No. 0704-0188

Public reporting burden for the collection of information is estimated to average 1 hour per response, including the time for reviewing instructions, searching existing data sources, gathering and maintaining the data needed, and completing and reviewing the collection of information. Send comments regarding this burden estimate or any other aspect of this collection of information, including suggestions for reducing this burden, to Washington Headquarters Services, Directorate for Information Operations and Reports, 1215 Jefferson Davis Highway, Suite 1204, Arlington VA 22202-4302. Respondents should be aware that notwithstanding any other provision of law, no person shall be subject to a penalty for failing to comply with a collection of information if it does not display a currently valid OMB control number.

| | | | | | |
|--|------------------------------------|-------------------------------------|----------------------------|---|---------------------------------|
| 1. REPORT DATE 2006 | | 2. REPORT TYPE | | 3. DATES COVERED 00-00-2006 to 00-00-2006 | |
| 4. TITLE AND SUBTITLE 2D semiconductor device simulations by WENO-Boltzmann schemes: efficiency, boundary conditions and comparison to Monte Carlo methods | | | | 5a. CONTRACT NUMBER | |
| | | | | 5b. GRANT NUMBER | |
| | | | | 5c. PROGRAM ELEMENT NUMBER | |
| 6. AUTHOR(S) | | | | 5d. PROJECT NUMBER | |
| | | | | 5e. TASK NUMBER | |
| | | | | 5f. WORK UNIT NUMBER | |
| 7. PERFORMING ORGANIZATION NAME(S) AND ADDRESS(ES) Division of Applied Mathematics, Brown University, Providence, RI, 02912 | | | | 8. PERFORMING ORGANIZATION REPORT NUMBER | |
| 9. SPONSORING/MONITORING AGENCY NAME(S) AND ADDRESS(ES) | | | | 10. SPONSOR/MONITOR'S ACRONYM(S) | |
| | | | | 11. SPONSOR/MONITOR'S REPORT NUMBER(S) | |
| 12. DISTRIBUTION/AVAILABILITY STATEMENT Approved for public release; distribution unlimited | | | | | |
| 13. SUPPLEMENTARY NOTES The original document contains color images. | | | | | |
| 14. ABSTRACT | | | | | |
| 15. SUBJECT TERMS | | | | | |
| 16. SECURITY CLASSIFICATION OF: | | | 17. LIMITATION OF ABSTRACT | 18. NUMBER OF PAGES 47 | 19a. NAME OF RESPONSIBLE PERSON |
| a. REPORT unclassified | b. ABSTRACT unclassified | c. THIS PAGE unclassified | | | |

1 Introduction

Electron transport in semiconductors, with space inhomogeneities at a tenth micron scale orders under long range interactions due to strong applied bias, needs to be modelled by meso-scale statistical models. One such type of models is the semi-classical approximation given by the Boltzmann Transport Equation (BTE) for semiconductors:

$$\frac{\partial f}{\partial t} + \frac{1}{\hbar} \nabla_{\mathbf{k}} \varepsilon \cdot \nabla_{\mathbf{x}} f - \frac{\mathbf{e}}{\hbar} \mathbf{E} \cdot \nabla_{\mathbf{k}} f = Q(f). \quad (1.1)$$

Following standard notation for statistical descriptions of electron transport [21, 25], f represents the electron probability density function (**pdf**) in phase space \mathbf{k} at the physical location \mathbf{x} and time t . Physical constants \hbar and \mathbf{e} are the Planck constant divided by 2π and the positive electric charge, respectively. The energy-band function ε is given by a non-negative continuous function of the form

$$\varepsilon(\mathbf{k}) = \frac{1}{1 + \sqrt{1 + 2 \frac{\tilde{\alpha}}{m^*} \hbar^2 |\mathbf{k}|^2}} \frac{\hbar^2}{m^*} |\mathbf{k}|^2, \quad (1.2)$$

in the Kane non-parabolic band model. Here, m^* is the effective mass and $\tilde{\alpha}$ is the non-parabolicity factor. Thus, by setting $\tilde{\alpha} = 0$ in equation (1.2) the model is reduced to the widely used parabolic approximation.

Our model takes into account the electrostatics produced by the electrons and the dopants in the semiconductor. Therefore, the electric field \mathbf{E} is self consistently computed by

$$\nabla_{\mathbf{x}} [\epsilon_r(\mathbf{x}) \nabla_{\mathbf{x}} V] = \frac{\mathbf{e}}{\epsilon_0} [\rho(t, \mathbf{x}) - N_D(\mathbf{x})], \quad (1.3)$$

$$\mathbf{E} = -\nabla_{\mathbf{x}} V, \quad (1.4)$$

where ϵ_0 is the dielectric constant in a vacuum, $\epsilon_r(\mathbf{x})$ labels the relative dielectric function depending on the material, $\rho(t, \mathbf{x}) = \int_{\mathbb{R}^3} f(t, \mathbf{x}, \mathbf{k}) d\mathbf{k}$ is the electron density, $N_D(\mathbf{x})$ is the doping and V is the electric potential. Eqs. (1.1)-(1.3)-(1.4) give the Boltzmann-Poisson system for electron transport in semiconductors.

Regarding the collision term $Q(f)$, the most important interactions in Si are due to scattering with lattice vibrations of the crystal, and particularly, those due to the acoustic and optical non-polar modes. Thus, the collision term will read as

$$Q(f)(t, \mathbf{x}, \mathbf{k}) = \int_{\mathbb{R}^3} [S(\mathbf{k}', \mathbf{k}) f(t, \mathbf{x}, \mathbf{k}') - S(\mathbf{k}, \mathbf{k}') f(t, \mathbf{x}, \mathbf{k})] d\mathbf{k}', \quad (1.5)$$

where the kernel S is defined by

$$S(\mathbf{k}, \mathbf{k}') = K_0(\mathbf{k}, \mathbf{k}') \delta(\varepsilon(\mathbf{k}') - \varepsilon(\mathbf{k})) + K(\mathbf{k}, \mathbf{k}') [(\mathbf{n}_q + 1) \delta(\varepsilon(\mathbf{k}') - \varepsilon(\mathbf{k}) + \hbar\omega_p) + \mathbf{n}_q \delta(\varepsilon(\mathbf{k}') - \varepsilon(\mathbf{k}) - \hbar\omega_p)]. \quad (1.6)$$

Here, we have taken into account acoustic phonon scattering in the elastic approximation and optical non-polar phonon scattering with a single frequency $\hbar\omega_p$. The phonon occupation factor \mathbf{n}_q is given by

$$\mathbf{n}_q = \left[\exp\left(\frac{\hbar\omega_p}{k_B T_L}\right) - 1 \right]^{-1},$$

where k_B is the Boltzmann constant and T_L is the constant lattice temperature. The symbol δ indicates the usual Dirac distribution.

From the distribution function f one evaluates its moments, namely, density $\rho(t, \mathbf{x})$, mean velocity

$$\mathbf{u}(t, \mathbf{x}) = \frac{1}{\rho(t, \mathbf{x})} \int_{\mathbb{R}^3} \frac{1}{\hbar} (\nabla_{\mathbf{k}} \varepsilon) f(t, \mathbf{x}, \mathbf{k}) d\mathbf{k}, \quad (1.7)$$

and mean energy

$$\mathcal{E}(t, \mathbf{x}) = \frac{1}{\rho(t, \mathbf{x})} \int_{\mathbb{R}^3} \varepsilon(\mathbf{k}) f(t, \mathbf{x}, \mathbf{k}) d\mathbf{k}. \quad (1.8)$$

In this paper, we continue our research to find suitable deterministic solvers for the Boltzmann-Poisson system of semiconductors. In particular, we demonstrate the capability of our WENO-BTE scheme [3] in giving reliable results for 2D realistic devices. We consider MESFET and MOSFET devices which have served as benchmarks for several other approximating models to device transport simulation, such as hydrodynamic, drift-diffusion, and energy transport solvers that have typically been compared to Monte Carlo results for solving the BTE [1, 7]. We refer to [8, 6, 9] for previous and alternative attempts for developing 1D deterministic solvers for BTE.

We show that the results of our deterministic solver WENO-BTE agrees remarkably well with the ones obtained by the Monte Carlo approach in the areas of the device in which there are enough particles to obtain sufficient statistics for particles. The main advantage of the WENO-BTE solver comes from its suitability to describe almost-empty areas of the device, where it is quite hard for Monte Carlo techniques to obtain relevant information on density, mean velocity and energy. These almost-empty regions are typically caused by the strong fields repelling the electrons near the gate/drain regions.

In addition, deterministic solvers provide a tool to compute accurate transient calculations of strong non-statistical equilibrium states as was already shown in [3] for one space

dimensional solvers simulating diodes. Our simulations for the two dimensional case indicate that one observes stabilization of moments in time and thus, we use small time variations of the density, current and energy as the code stopping criteria. A parallelization of the code for a fine grid has produced numerical evidence ensuring that stable states are obtained in higher dimensions as well [20] (see the 2D MESFET transient simulations by parallelized WENO-Boltzmann schemes in <http://kinetic.mat.uab.es/~carrillo/gallery1.html>).

In addition, deterministic solvers allow for the explicit computation of the probability density function solution f to the BTE transport model, and thus, all moments are computed with a better accuracy compared to Monte Carlo codes. Therefore, closure assumptions typically used in hydrodynamic systems can be validated numerically with our tools, as well as reliable code hybridization approaches linking kinetic to hydrodynamics under long range interactions, by identifying appropriate stiff regimes where hydrodynamic asymptotics are achieved. Consequently, our deterministic solvers can be considered as the real benchmark for moment-based transport solvers: hydrodynamic [1], drift-diffusion, energy-transport models [7] and so on; instead of Monte Carlo results.

Following the main ideas of [19, 2, 3], we have introduced in our previous work [4] a suitable dimensionless formulation by a change of variables in the wave vector \mathbf{k} that translates the original Boltzmann equation (1.1) in 2D into the following system: we use the coordinate transformation for the momentum vector \mathbf{k}

$$\mathbf{k} = \frac{\sqrt{2m^*k_B T_L}}{\hbar} \sqrt{\omega} \sqrt{1 + \alpha_K \omega} \left(\mu, \sqrt{1 - \mu^2} \cos \phi, \sqrt{1 - \mu^2} \sin \phi \right) \quad (1.9)$$

where $\alpha_K = k_B T_L \tilde{\alpha}$, $\omega \geq 0$ is a dimensionless energy, $\mu \in [-1, 1]$ is the cosine of the angle with respect to the x -axis and $\phi \in [0, 2\pi]$ is the azimuthal angle, respectively. We consider a two dimensional problem in the physical space and we define

$$\Phi(t, x, y, \omega, \mu, \phi) = s(\omega) \tilde{f}(t, x, y, \omega, \mu, \phi) ,$$

where $s(\omega) = \sqrt{\omega(1 + \alpha_K \omega)}(1 + 2\alpha_K \omega)$ is, apart a dimensional constant factor, the Jacobian of the transformation of coordinates (1.9) and \tilde{f} corresponds to the distribution function f after the change of variable (1.9). The use of the dimensionless unknown Φ instead of the distribution function f allows us to write the dimensionless Boltzmann equation in conservative form as

$$\frac{\partial \Phi}{\partial t} + \frac{\partial}{\partial x}(a_1 \Phi) + \frac{\partial}{\partial y}(a_2 \Phi) + \frac{\partial}{\partial \omega}(a_3 \Phi) + \frac{\partial}{\partial \mu}(a_4 \Phi) + \frac{\partial}{\partial \phi}(a_5 \Phi) = s(\omega) C(\Phi), \quad (1.10)$$

where the new collision operator $C(\Phi)$ and the flux functions a_i were computed in [4] and are repeated here for the sake of the reader: the flux functions a_i are given by

$$\begin{aligned}
a_1(\omega) &= \frac{1}{t_*} \frac{\mu s(\omega)}{(1 + 2\alpha_\kappa \omega)^2} \\
a_2(\omega, \mu, \phi) &= \frac{1}{t_*} \frac{\sqrt{1 - \mu^2} s(\omega) \cos \phi}{(1 + 2\alpha_\kappa \omega)^2} \\
a_3(t, x, y, \omega, \mu, \phi) &= -\frac{1}{t_*} \frac{2s(\omega)}{(1 + 2\alpha_\kappa \omega)^2} \left[E_x(t, x, y) \mu + E_y(t, x, y) \sqrt{1 - \mu^2} \cos \phi \right] \\
a_4(t, x, y, \omega, \mu, \phi) &= -\frac{1}{t_*} \frac{1 + 2\alpha_\kappa \omega}{s(\omega)} \sqrt{1 - \mu^2} \left[E_x(t, x, y) \sqrt{1 - \mu^2} - E_y(t, x, y) \mu \cos \phi \right] \\
a_5(t, x, y, \omega, \mu, \phi) &= \frac{E_y(t, x, y)}{t_*} \frac{\sin \phi}{\sqrt{1 - \mu^2}} \frac{1 + 2\alpha_\kappa \omega}{s(\omega)},
\end{aligned}$$

and the dimensionless collision operator $C(\Phi)$ is given by

$$\begin{aligned}
C(\Phi)(t, x, y, \omega, \mu, \phi) &= \\
&\frac{1}{2\pi t_*} \int_0^\pi \int_{-1}^1 [\beta \Phi(t, x, y, \omega, \mu', \phi') + a \Phi(t, x, y, \omega + \alpha, \mu', \phi') + \Phi(t, x, y, \omega - \alpha, \mu', \phi')] d\phi' d\mu' \\
&- \frac{1}{s(\omega) t_*} [\beta s(\omega) + a s(\omega - \alpha) + s(\omega + \alpha)] \Phi(t, x, y, \omega, \mu, \phi).
\end{aligned}$$

The constant parameters t_* , a and β depend on the scattering mechanisms. The constant α is the dimensionless phonon energy and the energy mesh has to be chosen properly for computational simplification of the collision kernel computation. For all details and physical constants we refer to works [2, 3, 4].

Let us remark that preliminary results of 2D Si MESFET devices were presented in [4] and that very fine grid results of a 2D Si MESFET and its transients were reported in [20] based on a parallelization of the numerical code we will present in this work. Our main objective in this work is to clarify the implementation of boundary conditions for the deterministic and for the Monte Carlo numerical scheme, explain the appearance of singularities in the electric field and demonstrate the overall excellent behavior of the deterministic code through the good agreement between the Monte Carlo results and the coarse grid results of our deterministic WENO-BTE scheme.

The structure of the paper is as follows. In the next section, we describe the numerical implementation of the kinetic boundary conditions used within the deterministic computation and we summarize the main characteristics of the deterministic scheme previously discussed in [4]. We also discuss the deterministic simulation of the 2D MESFET and

MOSFET, including its efficiency, accuracy and performance in this section. In Section 3, we give a presentation of the Monte Carlo method that has been used to compare to the deterministic scheme. Finally, we draw our conclusions in Section 4. Our presentation in Sections 2 and 3 will be based on the particular configuration of the MESFET device [16], since it contains all the main difficulties we will deal with, and we will present the results for the MOSFET [25] as a mere application of all the knowledge and difficulties faced and solved in the MESFET case.

2 2D deterministic device simulations

We describe the electron transport in a MESFET by solving the initial boundary value problem associated to equations (1.3), (1.4) and (1.10) in a spatial rectangular domain denoted by $\mathbf{R} = [0, x_0] \times [0, y_0]$ (see Figure 1) and with all \mathbb{R}^3 as the phase-velocity space. Our first objective in this section is to describe in detail the boundary conditions and its numerical implementation.

2.1 Boundary conditions for the BTE-Poisson system

We describe now the boundary conditions we have used to simulate both MESFET and MOSFET geometries by following classical assumptions for the modelling of two dimensional devices [21, 25].

At the source and drain contact regions, numerical boundary conditions must approximate neutral charges.

At the gate area, the numerical boundary condition yields an estimated incoming mean velocity which represents a transversal electric field effect due to the gate contact (see the electric field in Figure 3). These boundary conditions are imposed in an outside buffer layer above the contact and gate areas. As in classical simulations of hyperbolic systems with methods such as WENO schemes for flux reconstruction, these inflow conditions consist of the approximation of incoming flow on characteristic lines that cross the boundary towards the interior of the domain. That means these conditions are consistent with the well-posedness of the initial boundary value problem of the corresponding BTE-Poisson system.

Insulating conditions are imposed in the remainder boundary of the device.

Even though the existence of solutions to the initial-boundary value problem related to our continuum model is open, our simulation indicates that the solution is regular in the interior of the domain and may develop boundary singularities at the junctions of the contacts and insulating walls. In addition, these singularities are consistent with the same type of behavior for boundary problems for elliptic and parabolic equations with boundary junctions of Dirichlet and Neumann type conditions, which are described below.

As for the boundary conditions associated to the electrostatic potential, (i.e. solutions of the Poisson equation (1.3)-(1.4)), we impose classical boundary conditions for elliptic solvers associated to two-dimensional devices. They are as follows: prescribed potential (Dirichlet type conditions) at the source, drain, and gate contacts, and insulating (homogeneous Neumann conditions) on the remainder of the boundary.

Let us denote by $\partial\mathbf{R} = \partial\mathbf{R}_D \cup \partial\mathbf{R}_N$, the boundary of the device which we separate into $\partial\mathbf{R}_D$ for the gates and contact areas, and $\partial\mathbf{R}_N$ for the insulated areas. In particular the top boundary $(x, y_0); x \in [0, x_0]$ contains the source, drain and gate contacts. In classical modelling of micro-electronic devices, the doping function $N_D(\mathbf{x}) = N_D(x, y)$ is only defined in the semi-conducting domain \mathbf{R} . It is assumed to be a piecewise constant function, with jump surfaces separating un-doped regions, denoted by $n(x, y)$, where the background density is just given by bulk material properties, from strongly doped regions, denoted by $n^+(x, y)$, where density of background electrons has been increased to higher concentrations than the ones corresponding to bulk material. Source and drain contact boundary regions must satisfy $N_D(\mathbf{x}) = n^+(x, y)$, that is, are boundary regions located on areas of high background concentration.

More specifically, the boundary conditions imposed to the numerical probability density function (**pdf**) approximating the solution of the BTE, are as follows:

Source and drain contacts: We employ a buffer layer of ghost points outside both the MESFET and MOSFET domain in these contact areas. For $\{y = y_0\}$ and $\Delta y > 0$,

$$\hat{f}(t, x, y_0 + \Delta y, \mathbf{k}) = \frac{N_0(x)}{\int_{\mathbb{R}^3} \hat{f}(t, x, y_0, \mathbf{k}') d\mathbf{k}'} \hat{f}(t, x, y_0, \mathbf{k}) \quad (2.1)$$

where $N_0(x) = N_D(x, y_0)$ is the doping profile and $\hat{f}(t, x, y_0, \mathbf{k})$ denotes the evaluation of the numerical solution on mesh points located at $(t, x, y_0, \mathbf{k}(\omega, \mu, \phi))$, where x lies in those intervals such that the pair (x, y_0) is either a point in the source or drain boundary region.

Under the assumption that highly doped regions $n^+(x, y)$ are slowly varying (i.e. of very small total variation norm), the corresponding small Debye length asymptotics yields

neutral charges away from the endpoints of the contact boundary regions. Consequently, the total density $\rho(t, x, y_0)$ (zero order moment) and its variation takes asymptotically, in Debye length, the values of $n^+(x, y)$ away from the contact endpoints. This is the well-known limit for Drift Diffusion systems [21], and we observe that this is also the case for the kinetic problem, provided the kinetic solution satisfies approximately neutral charge conditions at these contact boundaries.

Thus, under the assumption that $n^+(x, y)$ is sufficiently large and that $|\nabla_y n^+(x, y)|$ is small, the Debye asymptotics near the source and drain contacts must yield $\rho \approx n^+$ and $|\nabla_y \rho| \approx |\nabla_y n^+|$, so $\rho(x, y)$ has bounded first order partial- y derivative at y_0 for (x, y_0) a point in the interior of the contact boundary.

In particular, a simple calculation shows that condition (2.1) yields neutral charges at these source and drain boundary regions. Indeed, integrating in velocity space both sides of the identity (2.1), for $\rho(t, x, y_0) = \int_{\mathbb{P}^3} f(t, x, y_0, \mathbf{k}) d\mathbf{k}$

$$\rho(t, x, y_0 + \Delta y) = N_0(x)$$

or, equivalently,

$$\begin{aligned} \rho(t, x, y_0) &\approx N_0(x, y_0) - \Delta y \nabla_y \rho(t, x, y_0) \approx \\ N_0(x, y_0) - \Delta y \nabla_y N_0(x, y_0) &\approx N_0(x, y_0) + o(\eta) \end{aligned} \quad (2.2)$$

where $\eta = \eta(\Delta y, \lambda, \|N_0\|_{C^1})$, and λ the scaled Debye length parameter associated to the contact area for highly doped regions.

Gate contact: We first describe the boundary condition for the MESFET simulation. Here we set a condition that yields an incoming mean velocity entering through the gate which is equivalent to decaying density in space and time due to the conservation of charge. Thus we set

$$\hat{f}(t, x, y_0 + \Delta y, \mathbf{k}) = \kappa \hat{f}(t, x, y_0, \mathbf{k}), \quad (2.3)$$

then, again integrating in velocity space both sides of the identity (2.3),

$$\nabla_y \rho(t, x, y_0) \approx \frac{\kappa - 1}{\Delta y} \rho(t, x, y_0). \quad (2.4)$$

In fact, boundary condition (2.4), which is of Robin (or mixed) type, is the natural simulation of a gate contact in an oxide region. The quantity $(\kappa - 1)/\Delta y$ must reflect the scale of the electric field flux across the interface corresponding to the gate voltage. This

quantity is related to the quotient of the permittivity and thickness of the gate region where charges are assumed negligible (oxide).

In order to explain this effect, we recall classical asymptotics corresponding to *thin shell* elliptic and parabolic type problems with Dirichlet data in the *thin outer shell* domain and a core larger-scale domain, where classical transmission conditions link both domains. The two dimensional asymptotic boundary condition for the Poisson system linking the oxide and semiconductor region yielding a Robin type condition was rigorously studied in [11, 12] and is given by

$$\nabla V \cdot \boldsymbol{\eta} = \frac{1}{2\pi \epsilon} \frac{\epsilon_{ox}}{\delta} \left(V - V_{gate} - \frac{\delta^2}{3} \right) \quad (2.5)$$

where $\boldsymbol{\eta}$ denotes the outer unit-vector to the interface surface given by the intersection of the boundaries to the oxide and the semiconductor regions. The value V_{gate} is the prescribed electrostatic potential at the gate contact and ϵ_{ox} and δ are the prescribed oxide permittivity and thickness respectively. This means the prescribed gate voltage V_{gate} is on the edge of the ϵ_{ox} -gate at δ -distance from the semiconducting domain.

Therefore, in the asymptotic limit where $0 < \epsilon_{ox}/\delta = C < \infty$ as both $\epsilon_{ox} \rightarrow 0$ and $\delta \rightarrow 0$, condition (2.5) becomes

$$-\mathbf{E} \cdot \boldsymbol{\eta} = \nabla V \cdot \boldsymbol{\eta} = \frac{1}{2\pi \epsilon} \frac{\epsilon_{ox}}{\delta} (V - V_{gate}). \quad (2.6)$$

which is a Robin type boundary condition for the Poisson equation at the oxide-semiconductor interface. This asymptotic boundary condition, formally derived for drift-diffusion equations by the computational electronic community, have been widely used in device simulations (see [22] and references therein).

Hence, in our present setting, one can interpret the relation (2.4) as a choice of an electric field flux rate $\frac{1-\kappa}{\Delta y}$ across the gate interface, where Δy is chosen a multiple of the oxide thickness, $\Delta y \approx \tilde{\kappa} \delta$ and then κ is chosen

$$\kappa \approx 1 + \frac{\epsilon_{ox} \tilde{\kappa}}{2\pi \epsilon} (V - V_{gate}), \quad (2.7)$$

when V is available.

Then condition (2.4) becomes, after combining with (2.6) and (2.7),

$$\nabla_y \rho(t, x, y_0) \approx -E_y \rho(t, x, y_0), \quad -E_y = -\mathbf{E} \cdot \boldsymbol{\eta} = \frac{\kappa - 1}{\Delta y} \quad (2.8)$$

which coincides with a classical macroscopic boundary condition for a density ρ that evolves according to a drift-diffusion equation. In general, the value V_{gate} is a prescribed gate voltage

and V is the computed value of the voltage in the gate interface for the Poisson solver in a semiconductor-oxide region with boundary conditions.

We remark that our MESFET simulations do not solve Poisson equation (1.3) using the asymptotic boundary condition (2.6) for small δ -thick gate/oxide region. The main reason is that we are neglecting the oxide region, and consequently we need to impose the value of the potential at the gate to be V_{gate} and fix some boundary condition for the distribution function f . Instead, in order to compensate the field flux across the gate interface, we having fixed $\kappa = 0.5$ and Δy a unit of mesh size. This choice is asymptotically equivalent to have fixed V on the MESFET gate region depending on V_{gate} and the oxide thickness δ in such a way that $\Delta y = \tilde{\kappa} \delta$, so that

$$-\frac{1}{2} = \kappa - 1 \approx \frac{\epsilon_{\text{ox}} \tilde{\kappa}}{2\pi \epsilon} (V - V_{\text{gate}}) \quad \text{or equivalently} \quad V \approx V_{\text{gate}} - \frac{\pi \epsilon}{\epsilon_{\text{ox}} \tilde{\kappa}}. \quad (2.9)$$

In particular, the choice of the parameter κ yields an approximation that may modify the effective field flux across the gate contact. In fact this choice may be interpreted as a calibrating parameter to evaluate the strength of the electric field flux across the gate/oxide interface when Dirichlet data V_{gate} has been prescribed instead of either the Robin type data (2.6) or the more accurate simulation of the Poisson solver in the whole oxide/semiconductor domain.

Finally, for the MOSFET simulation the gate contact, we recall that the Poisson solver imposes a Dirichlet condition by prescribing V_{gate} and since the gate contact is outside the domain of the transport equation, no condition is needed for the computation of the probability density function **pdf**.

Insulating walls: In the remainder of the boundary region, we impose classical elastic specular boundary reflection. For $\mathbf{x} \in \partial\mathbf{R}_N$

$$f(t, \mathbf{x}, \mathbf{k}) = f(t, \mathbf{x}, \mathbf{k}^*) \quad \text{for } \mathbf{k} \cdot \boldsymbol{\eta}(\mathbf{x}) < 0 \quad \text{with } \mathbf{k}^* = \mathbf{k} - 2\mathbf{k} \cdot \boldsymbol{\eta}(\mathbf{x}) \quad (2.10)$$

$$\frac{\partial V}{\partial \boldsymbol{\eta}}(t, \mathbf{x}) = 0. \quad (2.11)$$

Oxide/semiconductor MOSFET interface: The Poisson equation is posed with neutral charges in the oxide region and (1.3) in the semiconducting region. Condition (2.10) is imposed on the oxide/semiconductor interface and the electric field on this interface is computed from the Poisson solver.

2.2 Singular boundary behavior.

2.2.1 MESFET geometry.

At the boundary region $y_0 = 0.2\mu m$, we have contact/insulating and insulating/gate changes of the boundary condition. It is well-known that solutions of the Poisson equation develop singularities under these conditions. Namely, when solving the Poisson equation in a bounded domain, with a Lipschitz boundary and a boundary condition that changes type from Dirichlet to homogeneous Neumann or Robin type data on both sides of a conical wedge, with an angle $0 \leq \vartheta \leq 2\pi$, whose vertex is at the point of data discontinuity, the solution will develop a singularity at the vertex point depending on the angle ϑ .

More specifically, for an elliptic problem in a domain with data-type change, the solution remains bounded with a radial behavior of a power less than one if $\pi/2 \leq \vartheta \leq 2\pi$. Its gradient then becomes singular (see for instance Grisvard [14] for a survey on boundary value problems of elliptic PDE's in a non-convex domain).

In this case, it is possible to prove the corresponding asymptotic behavior is controlled from above and below by functions with bounded Laplacian whose radial component is of order $O(r^{\pi/2\vartheta})$. More precisely, a local control function (barrier) to solutions of Laplace's equations with bounded right hand side can be constructed by taking functions of the form $r^\tau \sin(\tau b) + C_o$ with $\tau = \frac{\pi}{2\vartheta}$.

In the particular case of the jump of a boundary condition in a *flat boundary surface* (*zero curvature*), such as in the boundary given by $y_0 = 0.2$, the angle is $\vartheta = \pi$ which makes the electric potential $V = r^{1/2} \sin(b/2) + C_o$. Then its gradients (i.e. the components of electric field) develop a singularity of the order $\nabla V \approx Mr^{-1/2}$. Similar local asymptotic behavior occurs for parabolic systems in bounded domains with discontinuous boundary data operators.

We remark that our calculations resolve this singular boundary behavior as is demonstrated in Figures 2 and 3.

Consequently, elliptic and parabolic descriptions of the density flow at the drift-diffusion level remain with the same singular boundary behavior, even though mobilities functions are saturated quantities; that is, they are bounded functions of the magnitude of the electric field [12]. In fact, these conditions have been used for two dimensional drift-diffusion simulations of MESFET devices and this singular boundary behavior was obtained [5].

In view of this boundary asymptotic behavior at the macroscopic level and the numerical results we obtain for the deterministic solutions of the BTE-Poisson system and its moments (see Figures 2 and 3), we conjecture that the moments of the particle distribution function $f(t, \mathbf{x}, \mathbf{k})$ have *the same spatial asymptotic behavior as the density solution of the drift diffusion problem* at the boundary points with a discontinuity in the data. In other words, the collision mechanism preserves the spatial regularity of the **pdf** as though its zeroth moment would satisfy the drift-diffusion equations, even though the numerical evidence indicates that the average of the **pdf** (i.e. density) will not evolve according to such a simple macroscopic model.

Based in our calculations in Figures 2 and 7, we conjecture the density $\rho(t, \mathbf{x})$ develops a contact local singularity *of the same asymptotic order as the electrostatic potential $V(t, \mathbf{x})$ at (t, x, y_0)* . In particular, under the assumption that the first and second moments of the $f(t, \mathbf{x}, \mathbf{k})$ are bounded in (t, \mathbf{x}) , local behavior of the mean velocity $u(t, \mathbf{x})$ defined in (1.7) compares to the one of the electric field $\mathbf{E}(t, \mathbf{x})$, and thus

$$|\mathbf{u}(t, x, y_0)| \approx Mr^{-1/2} \quad (2.12)$$

with r the distance from (x, y) to the vertex where the data jumps. Similarly, the mean energy $\mathcal{E}(t, x, y_0)$, defined in (1.8), develops a singularity of the same order as the mean velocity in (2.12).

2.2.2 MOSFET geometry.

In this particular case, the electron **pdf** transport is modelled only in the semiconducting region with insulation conditions along the oxide/semiconductor interface. The first five moments are expected to be bounded along the interface (see Figure 11). The only points where singularities generating singular electric fields could arise for the Poisson solver are the points where the $n^+ - n$ junctions meet the semiconductor-oxide interface. We observe that, in fact, the maximum value for the energy (second moment for the **pdf**) occurs at the $n - n^+$ drain junction.

Indeed, it has been shown in [10] that all second derivatives of the potential will remain bounded at those intersections, provided the boundary condition along the interface are of transmission or insulating type for a drift-diffusion model. From our calculations (see Figure 11), we expect similar behavior for the spatial regularity of the moments associated to the kinetic solution as well, which in these case, would yield bounded mean velocities implying bounded energy throughout the semiconducting device domain.

2.3 The WENO-BTE solver

We adopt the same fifth order finite difference WENO scheme coupled with a third order TVD Runge-Kutta time discretization to solve (1.10) as that used in our previous work [3]. The fifth order finite difference WENO scheme was first designed in [17], and the third order TVD Runge-Kutta time discretization was first proposed in [24]. In our calculation, the computational domain in each of the five directions x , y , ω , μ and ϕ is discretized into a uniform grid, with $1 + N_x$, $1 + N_y$, N_ω , N_μ and N_ϕ points in these directions respectively. Our numerical method also allows the use of non-uniform but smooth grids in order to concentrate points near regions where the solution has larger variations. In the x and y directions, the computational boundaries are located at grid points. In the other three directions, the computational boundaries are located in the middle of two grid points in order to efficiently implement symmetry type boundary conditions to maintain conservation.

The approximations to the point values of the solution $\Phi(t^n, x_i, y_j, \omega_k, \mu_l, \phi_m)$, denoted by $\Phi_{i,j,k,l,m}^n$, are obtained with a dimension by dimension (not dimension splitting) approximation to the spatial derivatives using the fifth order WENO method in [17]. For example, when approximating $\frac{\partial}{\partial x}(a_1\Phi)$, the other four variables y , ω , μ and ϕ are fixed and the approximation is performed along the x line:

$$\frac{\partial}{\partial x}(a_1(\omega_k, \mu_l)\Phi(t^n, x_i, y_j, \omega_k, \mu_l, \phi_m)) \approx \frac{1}{\Delta x} (\hat{h}_{i+1/2} - \hat{h}_{i-1/2})$$

where the numerical flux $\hat{h}_{i+1/2}$ is obtained with a one dimensional procedure. We will not repeat the details of the computation for this numerical flux here and refer the reader to [3, 17, 23].

Next, we briefly describe the numerical implementation of the boundary conditions. See the previous subsection for more details of some of these boundary conditions.

- At $x = 0$ and $x = x_0$, we implement a reflective boundary condition by prescribing the values of the ghost points using for $x > 0$,

$$\Phi(t, -x, y, \omega, \mu, \phi) = \Phi(t, x, y, \omega, -\mu, \phi),$$

$$\Phi(t, x_0 + x, y, \omega, \mu, \phi) = \Phi(t, x_0 - x, y, \omega, -\mu, \phi).$$

At $y = 0$, we implement a similar reflective boundary condition using for $y > 0$,

$$\Phi(t, x, -y, \omega, \mu, \phi) = \Phi(t, x, y, \omega, \mu, 2\pi - \phi),$$

for the ghost points.

- For the top boundary $y = y_0$, the boundary conditions are explained in the previous subsection.
- At $\omega = 0$, the boundary condition is given to take into consideration that this is not really a physical boundary; however, a “ghost point” at (ω, μ, ϕ) for a negative ω is actually a physical point at $(-\omega, -\mu, 2\pi - \phi)$. We thus take the boundary condition for $\omega > 0$ to be,

$$\Phi(t, x, y, -\omega, \mu, \phi) = \Phi(t, x, y, \omega, -\mu, 2\pi - \phi).$$

An averaging is then performed for the fluxes for $\omega = 0$ to enforce conservation.

- The boundary region $\omega = \omega_{max}$ is taken as an outflow boundary with a Neumann type condition

$$\Phi(t, x, y, \omega, \mu, \phi) = \Phi(t, x, y, \omega_{max}, \mu, \phi), \quad \omega > \omega_{max}$$

and the explicit enforcement of $\hat{h}_{N_\omega+1/2} = 0$ for the last numerical flux in order to enforce conservation of mass.

- At $\mu = -1$ and $\mu = 1$, we take the boundary conditions for $\mu > 0$,

$$\Phi(t, x, y, \omega, -1 - \mu, \phi) = \Phi(t, x, y, \omega, -1 + \mu, \phi),$$

$$\Phi(t, x, y, \omega, 1 + \mu, \phi) = \Phi(t, x, y, \omega, 1 - \mu, \phi),$$

motivated by the physical meaning of μ as the cosine of the angle to the z -axis. We also explicitly impose $\hat{h}_0 = \hat{h}_{N_\mu+1/2} = 0$ for the first and last numerical fluxes in order to enforce conservation of mass.

- At $\phi = 0$ and $\phi = 2\pi$, we take the boundary conditions for $\phi > 0$,

$$\Phi(t, x, y, \omega, \mu, -\phi) = \Phi(t, x, y, \omega, \mu, \phi),$$

$$\Phi(t, x, y, \omega, \mu, 2\pi + \phi) = \Phi(t, x, y, \omega, \mu, 2\pi - \phi),$$

motivated by the physical meaning of ϕ as the angle around the z -axis. We also explicitly impose $\hat{h}_0 = \hat{h}_{N_\phi+1/2} = 0$ for the first and last numerical fluxes in order to enforce conservation of mass.

An integration to compute the various moments using the **pdf** is approximated by the composite mid-point rule:

$$\begin{aligned} & \int_0^{+\infty} d\omega \int_{-1}^1 d\mu \int_0^{2\pi} d\phi b(\omega, \mu, \phi) \Phi(t, x, y, \omega, \mu, \phi) \\ \approx & \sum_{m=1}^{N_\phi} \sum_{l=1}^{N_\mu} \sum_{k=1}^{N_\omega} b(\omega_k, \mu_l, \phi_m) \Phi(t, x, y, \omega_k, \mu_l, \phi_m) \Delta\omega \Delta\mu \Delta\phi \end{aligned}$$

which is at least second order accurate. This condition is even more accurate when Φ and some of its derivatives are zero at the boundaries, and, in fact, it is infinite order accurate or spectrally accurate for C^∞ functions with compact support. Notice that mass conservation is enforced with this integration formula and boundary conditions indicated previously.

The Poisson equation (1.3) for the potential V and the electric field (1.4) are solved by the standard central difference scheme, with the given V_{bias} boundary conditions at the source, drain and gate.

The time discretization is by the third order TVD Runge-Kutta method [24].

Finally, due to the explicit character of the time evolution solver we need to impose the standard CFL condition for these RK schemes. That is,

$$\Delta t \leq CFL \left(\frac{\Delta x}{\max(|a_1|)} + \frac{\Delta y}{\max(|a_2|)} + \frac{\Delta \omega}{\max(|a_3|)} + \frac{\Delta \mu}{\max(|a_4|)} + \frac{\Delta \phi}{\max(|a_5|)} \right) \quad (2.13)$$

where the maximum is taken over the grid points and we use $CFL = 0.6$ in the actual calculation. Note that we are taking $\max(|a_4|)$ over a grid without $\omega = 0$. For the cases we have run, the source collision term is not stiff enough to change the CFL condition determined by the approximations to the spatial derivatives. This CFL condition at first glance may seem severe, however some practical cases shown in next sections demonstrate this is not the case for coarse grids. This CFL condition does become more severe due to the appearance of the singularities in the force field for more refined meshes. Therefore, although the CPU time for coarse grids is comparable with DSMC simulations, fine grid high accurate deterministic results are more costly.

2.4 Deterministic simulation of a 2D Si MESFET

In Figures 2 and 3 we show the results of the macroscopic quantities for the MESFET when a grid of 43×25 points is used in space, 80 points in the energy ω , and 12 points in each of the angular μ and ϕ directions (grid A). The doping is $3 \times 10^{17} \text{ cm}^{-3}$ in the n_+ zone

and 10^{17} cm^{-3} in the n zone. We assume applied biases of $V_{source} = 0.V$, $V_{gate} = -0.8V$ and $V_{drain} = 1.V$. The velocity and electric vector fields give a clear picture of the electron transport in the device.

We demonstrate numerically that singularities appear in the electric field and the square-root behavior of the electric potential is clearly defined. The same behavior seems to be the case for the density and the velocity field but the spatial resolution is not good enough for a complete numerical answer to this point. The appearance of these singularities is a difficulty for the numerical resolution of this problem, since the CFL condition (2.13) becomes more restrictive due to the singularity of the electric field as the grid gets finer.

We observe highly accurate non-oscillatory behavior near junctions and expected high channel anisotropic energy near the gate drain region, where the two-dimensional effects are most significant. These assertions are also based on the results of the probability density functions in Figure 4. These **pdf's** have been obtained by averaging the computed values of Φ over the angle ϕ . We observe the overall smoothness of the **pdf** Φ function even near the gate-insulated data-type change regions.

We also show in Figures 5 and 6 the discrepancies between the results obtained with grid A and the results of two other grids: a coarser grid with 25×13 points in space, 40 points in the energy ω , 4 points in each of the angular μ and ϕ directions (grid B), and a finer grid with 91×33 points in space, 80 points in the energy ω and 12 points in each of the angular μ and ϕ directions (grid C). Figures 5 and 6 show in a compact way the scaled relative differences for density, electric current, electric field and potential, and the mean energy multiplied by the charge density. Measures of the discrepancies are given by the following formulas. Let q_{ij}^c be the value of an hydrodynamical quantity q^c at the grid point (x_i, y_j) obtained by using the coarse grid; q_{ij}^f is the corresponding value obtained by using the fine grid. Then,

$$d_{ij} = \frac{|q_{ij}^c - q_{ij}^f|}{\max\{q^f\} - \min\{q^f\}} \quad (i = 0, 1, \dots, N_x) \text{ and } (j = 0, 1, \dots, N_y) \quad (2.14)$$

and

$$d_j = \frac{1}{1 + N_x} \sum_{i=0}^{N_x} d_{ij} \quad (i = 0, 1, \dots, N_x). \quad (2.15)$$

These seem to be good functions to measure the dimensionless distance between the two surfaces. Here, $N_x + 1$ and $N_y + 1$ are the numbers of the fine grid points in the x and y directions, respectively. We use a simple linear interpolation in order to obtain the values of the quantity q^c at those points belonging to the fine grid but not to the coarse grid.

We can see that the results of the grid A and grid B already agree reasonably well, even though the grid B has only as few as 4 points in some directions. The relative error is in general less than 5%, except for the region near $y = 0.2\mu m$ where the singularities exist and where the error could reach around 10% for the worst resolved quantity (horizontal momentum). This indicates that the code can be used on very coarse meshes with fast turn-around time to obtain engineering accuracy with average relative errors below 5%. The results of the grid A and grid C agree remarkably well overall. The relative error is in general well below 2%, except for the region near $y = 0.2\mu m$ where the singularities exist and the error could reach around 4.5% for the worst resolved quantity (horizontal momentum). The larger errors near $y = 0.2\mu m$ are caused by the fact that the singularities are not as well captured with the coarser grid as the smooth part of the solution. This can be seen in Figure 7. This is particularly important from a computational time point of view since the fine grid results have taken almost 2 weeks to achieve steady state at 5ps while the coarse grid takes less than an hour in a standard Pentium IV-2.4 GhZ PC. This extremely high computational cost of the fine grid is due to the restrictive CFL condition caused by singularities more than the increased number of grid points.

In order to reduce the computational time for the fine mesh, we introduce a limiter for the electric field through the formula

$$\mathbf{E}_{cut} = (\min\{\max\{E_x, -E_c\}, E_c\}, \min\{\max\{E_y, -E_c\}, E_c\}, 0) \quad (2.16)$$

where E_c is positive and fixed. In our simulation (grid \mathbf{E}_{cut}), we choose $E_c = 150$ (kV/cm) and the same grid of the case A. At each time step, we solve the Poisson equation and evaluate the true electric field \mathbf{E} , but use instead \mathbf{E}_{cut} in the force term of the Boltzmann equation. The discrepancies between the results of grid A and \mathbf{E}_{cut} are reported in Figure 8 and comparison results in Figure 9 show a remarkable agreement with respect to the original results at a much lower computational time.

2.5 Deterministic simulation of a 2D Si MOSFET

In this subsection we report the results of the simulation of a MOSFET whose geometry is sketched in Figure 10 in which the contacts are doped with an electron density given by $n_+ = 3 \times 10^{17} \text{ cm}^{-3}$. No doping is given in the n domain. Here, we have solved the Boltzmann-Poisson system disregarding completely the dynamics of the holes. The origin of the potential is set at the source and we consider applied biases of $V_{gate} = 0.4V$ at the gate and $V_{drain} = 1V$ at the drain respectively.

The steady state results are reported in Figures 11 and 12 which are quite clear about the qualitative transport of electrons through the device. The main difference with respect to the MESFET device relies on the fact that the singularities of the field and the square-root behavior of changing-data points on the electric potential are in the oxide region where the transport of electrons is not computed through the Boltzmann equation. Thus, the appearance of the singularities of the force field does not affect the CFL condition in the area in which the transport equation is solved. This makes MOSFET much easier to compute than MESFET in terms of CPU time. The results shown have been obtained with a grid of 49×33 points in space, 66 points in the energy ω and 12 points in each of the μ and ϕ directions, and have taken 3 days on a standard Pentium IV-2.4 GhZ PC.

Similar comments with respect to a comparison with coarser grids can be made in the case of a MOSFET. Although we do not show any figure to save space, coarse to fine grid comparisons have been performed and the conclusions of the MESFET remain valid. Thus, coarse grid BTE results are competitive in accuracy versus computational time with respect to DSMC results for a MOSFET device. Finally, we report in Figure 13 the **pdf's** Φ , averaged over ϕ , at different points of the device showing again the overall smoothness of the distribution function.

3 Comparisons with Monte Carlo results

The classical widespread method to investigate transport processes in semiconductor devices at the microscopic level is based on the Direct Simulation Monte Carlo (DSMC) method. The main advantage of this approach consists in the simple way to take into account different forces acting on the electrons. The dynamics of particles is well described by Newton's law when they move freely, driven by the mean electric field, and by a stochastic process during the collisions with phonons.

Although DSMC is a stochastic numerical method and the BTE equation is a deterministic equation, it has been shown in [26] that, for the classical case of space homogeneous mono-atomic elastic gases, the stochastic numerical method converges, in a probabilistic sense, to the solution of the BTE. This fact has led to a common acceptance on the equivalence of stochastic approaches to solve the BTE and their corresponding deterministic approximations, even in cases of strong space inhomogeneities.

Recent comparisons for Boltzmann-Poisson transport models [18] show an excellent agreement when spatially-homogeneous solutions (bulk case) are analyzed and its relevant

moments are compared. This confirms that collision and drift (for constant electric field) are well-described by both models. We stress that the same physical parameters were used in both models and, in particular, the scattering rates coincide exactly. In particular, when inhomogeneous solutions [3, 18] are considered, the agreement between hydrodynamical quantities is usually good for small relative energies, but not always excellent.

In order to understand the origin of these discrepancies, it is useful to recall two aspects of DSMC methods. The first one, which relates to the boundary conditions, is the rule that is used when an electron must be injected into the device. The second one relates to the length of the free flight time. Since there is not a unique resolution to these two issues [15, 13] different choices give often inconsistent results when comparisons that involve these type of stochastic methods are made. These facts are well-known in the DSMC community. However, we find it useful to discuss these two factors in more detail in order to make clear the comparison criteria between stochastic DSMC and deterministic BTE numerical solutions and to explain the source of their differences.

We first consider the boundary issue for the stochastic DSMC method. Since the electrons can exit from the interior of the device (for instance, through the drain or source contacts in the MESFET or MOSFET geometry), the total density of charges may decrease. Hence, we must decide whether to inject electrons to balance this loss. For spatially homogeneous solutions where charge must be conserved, this is a simple problem to address. However, for general geometries with strong space inhomogeneities, the difficulty in treating the electron injection issue arises since electrons flow through metallic contacts, which are also connected to a circuit. In principle, a full treatment of the system consisting of both the device and the circuit would solve the problem completely. Such simulation, however, can be attained only in very simple cases.

Therefore we must resort to some reasonable rule which might be justified by means of asymptotic analysis, physical considerations or empirical tests. In this context, a well-accepted starting point to decide how many particles must be injected is called *charge neutrality*. In practice, after every time step of DSMC, we consider the cells in the vicinity of the contacts, usually those including boundaries, where it is possible to inject electrons, and we evaluate the charge density in each of these cells.

In particular, we find that the charge density may be equal, greater or smaller than the doping density on every cell. In the first case no change is required; in the second we easily eliminate a few particles in order to get the right balance; in the last case, we have to supply electrons to balance the loss of charge. This electron injection represents a crucial

point, since we must decide how to choose the velocity of the entering particles (position can be chosen randomly inside every cell due to the stochastic nature of the simulation.)

There is no unique recipe for electron injection in order to balance charges. Simple common chosen rules [13] are based on the following distribution functions or methods:

- a) The global Maxwellian distribution $\exp(-\varepsilon/k_B T_L)$.
- b) A shifted semi-Maxwellian.
- c) A velocity-weighted Maxwellian distribution.
- d) The reservoir method.

For the first choice, the energy of the entering particles is given according to the Maxwellian distribution function and then the magnitude of the wave-vector $|\mathbf{k}|$ is determined. So, in order to fix \mathbf{k} , we need the values of the two angular variables which can be randomly chosen with the only constraint that the velocity of the electron is directed towards the interior of the device. This rule is reasonable when the mean current is almost zero near the contact which is the case for highly doped regions where the Debye length asymptotics dominates the transport due to field effects.

Concerning the case b), we must point out that the meaning of the shifted Maxwellian in the framework of semiconductor transport differs from those of classical perfect gases. If we assume the parabolic band approximation for the energy band structure, then the wave-vector \mathbf{k} can be seen as a classical particle velocity and a term as $\mathbf{k} - \mathbf{u}$ (\mathbf{u} being a fixed mean velocity) is a shifted velocity. Moreover, we can define also the electron temperature. However, caution is needed since a shifted Maxwellian is not a solution of the BTE except for the case in which only electron-electron interactions are considered. This means electron-phonon interactions are neglected and that the force field term in the free streaming operator takes into account only electron-doping interaction and the external electric field. When a non-parabolic band approximation is employed, we may continue the use of a shifted velocity, but the physical meaning of the factor inside the exponential function is not clear since it does not represent the kinetic temperature anymore. To overcome this problem, often the lattice temperature is used under the assumption that contacts are in thermal equilibrium with the crystal. Therefore, choice b) allows us to have a particle moving according to the mean electric current, but with an inaccurate energy. In fact, a shifted Maxwellian when used in hot electron situations such as strong

inelastic scattering *overestimates significantly the energy loss from electrons to phonons* and therefore *underestimates the electron mean energy*. Thus, the use of this assumption on the incoming distribution is reasonable only when electron-electron scattering is the dominant process. This is the case when the electron density is large enough (a value greater than $5 \cdot 10^{17} \text{ cm}^{-3}$ seems reasonable) and the electric field is not very strong.

Some comparisons between the BTE and DSMC results exhibit this effect in 1D diode simulations of channels under 400nm subject to relatively strong voltage bias. In reference [3] we implemented choice a). The agreement is excellent except in the case of a 50-nm channel diode, where a small difference in the curves concerning the hydrodynamical energy near the extreme of the diode is evident. In [18] the stochastic *Damocles* code was employed with a shifted Maxwellian. The DSMC and deterministic simulation results agree well for longer devices, but as the length of the channel is shorter, the behavior of the hydrodynamical variables differ clearly.

The case c) employs a distribution function, which, apart a normalizing factor, is the product of the global Maxwellian (with the lattice temperature) by the electron velocity. In ref. [13] an interesting application to a 1D Schottky-barrier diode shows a good performance of this choice. We note that all the cases a)-c) assume that the temperature at the contacts is very near to the lattice temperature and the shape of the distribution function of the entering particles is given. In our 2D simulations the appearance of the singularities near the extremes of the contacts suggests that the hypotheses concerning the temperature might not be accurate at these points. Hence, we believe that distributions a-c) are not always reasonable in these cases. Consequently, we employed the rule d) in this paper. We add a layer of ghost cells outside the device near the drain and source contact regions. Electrons move inside these cells under the electric field obtained by the simplest extrapolation formula using the nearest values of the true cells. Moreover, electrons encounter collisions with phonons.

We then apply the *charge neutrality* criterion only in the ghost cells and create new particles if necessary according to the rule a). In this way electrons moving from the ghost cells to the device enter with reasonable velocity and energy. In our DSMC simulation, this mechanism seems to perform better than the other approaches, even though the electric current near the contacts is not well described (see Figures 15 and 19). One of the reasons for this failure arises from the number of ghost cells added to the physical device. In fact, a small number guarantees the charge neutrality rule at the contacts, but the electric current might suffer from the low-energy entering particles. On the other hand, by increasing the number of the ghost cells, we improve the accuracy of the electric current but we get a

nonphysical behavior of the density profile. Finally, we also prefer to use rule d) because it is the most consistent with the boundary conditions which we use in the BTE simulations.

The accuracy of the deterministic simulations may be a useful tool to check the validity of the four rules a-d) in the case of 2D devices. Of course, this study requires a large number of simulations, using different values for the applied voltages, doping and geometry sizes in order to reach meaningful conclusions. This interesting research is out of the scope of the present work.

The second item mentioned above, i.e., the free flight duration, is based on the total scattering rate. There is a theoretical formula to evaluate this parameter.

We denote by $P[\mathbf{k}(t)]dt$ the probability that an electron in the state \mathbf{k} encounters a collision during the time interval dt . When considering the motion of this single electron, $\mathbf{k}(t)$ denotes the wave-vector \mathbf{k} as a function of the time t . Let $t = 0$ be the time of the last collision. Then, the probability $\mathcal{P}(t)$ that the electron will encounter its next collision during dt is given by

$$\mathcal{P}(t)dt = P[\mathbf{k}(t)] \exp \left[- \int_0^t P[\mathbf{k}(t')]dt' \right] dt. \quad (3.1)$$

We remark that we must use the above formula after every collision and for any particle, that is, if we consider another electron, then its motion will be different and therefore it will have a different probability $P[\mathbf{k}(t)]dt$. Moreover, it is evident that this procedure requires the knowledge of the function $P[\mathbf{k}(t)]$ as $t \rightarrow \mathbf{k}(t)$. This whole procedure is too costly for practical applications, and thus, simple approximations of the above formula have been proposed (see for instance [15]). In our simulations, we use the simplest rule given in [25]: fix the maximum value of the electron energy ε_{\max} , and define

$$\Gamma = \max_{\mathbf{k}} \left\{ \int_{\mathbb{R}^3} S(\mathbf{k}, \mathbf{k}') d\mathbf{k}' : \varepsilon(\mathbf{k}) \leq \varepsilon_{\max} \right\}.$$

Then approximate $P[\mathbf{k}(t)]$ from (3.1) with the constant Γ . So, we obtain

$$\mathcal{P} = \Gamma \exp(-t\Gamma).$$

Since $r = \mathcal{P}/\Gamma$ is a random number distributed uniformly between 0 and 1, we can choose the free flight duration t_r according to the rule

$$t_r = -\frac{1}{\Gamma} \log(r).$$

Therefore, every electron has a proper time t_r which is again generated after every collision drawing the random number r .

Numerical solutions obtained by using Boltzmann-Poisson system and DSMC are considered in the stationary regime where noise of the stochastic solutions are reduced. In Figure 14, the error formula (2.14) is employed to compare results between the BTE (grid A) and DSMC simulations for MESFET device. We also report BTE-DSMC comparison results of three cuts for fixed values of $y = 0.2\mu m$, $y = 0.175\mu m$ and $y = 0.1\mu m$ in Figures 15, 16 and 17 respectively.

These results show excellent agreement between the deterministic and the DSMC simulations, except in almost-empty regions (see Figure 15). Here, we are only stressing different values of the energy near the gate-boundary. The mean energy for DSMC is lower than the corresponding value obtained by the deterministic result. We believe that this fact depends on the energy of the injected electrons.

Moreover, energy curves corresponding to the DSMC simulation show unusual non physical oscillations at $y = 0.1\mu m$ near the boundary $x = 0$. Here the electric field is low and we believe that the deterministic result is very accurate. This seems to indicate that in these regions the free flight duration is inaccurate; hence electrons do not have a correct number of collisions with phonons, and the amount of their energy transferred to the lattice is also inaccurate. Analogous conclusions hold also in the case of a MOSFET; see Figures 18, 19, 20 and 21.

Both for the MESFET and the MOSFET device, the discrepancies between the DSMC and the deterministic results are important near the ohmic contacts. It is reasonable that a more refined Monte Carlo code is able to generate better hydrodynamical profiles. In this paper, we have focused our attention on solving the BTE equation deterministically and on using the DSMC scheme, based on the code described in [25], to check the accuracy, the performance of the deterministic numerical scheme and the agreement, except for small spatial regions, with stochastic solutions. We remark that the excellent agreement for grid points where the solution shows strong gradients confirms the absence of viscosity effects in WENO-scheme results.

4 Concluding remarks

We have adapted a high order accurate finite difference weighted essentially non-oscillatory (WENO) solver for the direct numerical simulation of two dimensional Boltzmann transport equation (BTE) coupled with a Poisson equation describing two dimensional semiconductor devices, including the MESFET and MOSFET devices. We have demonstrated the

performance of this solver through a comparison between coarse and fine grid simulations and through a comparison with the results obtained by a direct simulation Monte Carlo (DSMC) solver. We have clarified several issues related to the two dimensional devices including the implementation of boundary conditions, singularities, and factors important for the comparison between deterministic BTE and stochastic DSMC solvers. The simulation results demonstrate the superior capability of the WENO-BTE solver, which can be used to obtain accurate results with a very coarse mesh (with as few as 4 grid points in the angular directions).

Acknowledgments

Research of the first author is supported by the European IHP network “Hyperbolic and Kinetic Equations: Asymptotics, Numerics, Applications”, RNT2 2001 349 and DGI-MCYT/FEDER project BFM2002-01710. Research of the second author is supported by NSF grant DMS-0204568. Research of the third author is supported by the European IHP network “Hyperbolic and Kinetic Equations: Asymptotics, Numerics, Applications” and Italian COFIN 2004. Research of the last author is supported by ARO grant W911NF-04-1-0291 and NSF grant DMS-0207451. We thank the Institute of Computational Engineering and Sciences (ICES) at the University of Texas for partially supporting this research. We thank J.M. Mantas for many helpful comments, numerical results for grid C, discussions and figure-editing, and J. Proft for her careful reading and editing of this manuscript.

References

- [1] A.M. Anile, G. Mascali and V. Romano, *Recent developments in hydrodynamical modeling of semiconductors*, *Mathematical problems in semiconductor physics*, Lecture Notes in Math., **1823**, 1–56 (2003).
- [2] J.A. Carrillo, I.M. Gamba, A. Majorana and C.-W. Shu, *A WENO-solver for the 1D non-stationary Boltzmann–Poisson system for semiconductor devices*, *J. Comput. Electron.*, **1**, 365–370 (2002).
- [3] J.A. Carrillo, I.M. Gamba, A. Majorana and C.-W. Shu, *A WENO-solver for the transients of Boltzmann–Poisson system for semiconductor devices. Performance and comparisons with Monte Carlo methods*, *J. Comput. Phys.*, **184**, 498–525 (2003).

- [4] J.A. Carrillo, I.M. Gamba, A. Majorana and C.-W. Shu, *A direct solver for 2D non-stationary Boltzmann-Poisson systems for semiconductor devices: a MESFET simulation by WENO-Boltzmann schemes*, J. Comput. Electron., **2**, 375–380 (2003).
- [5] Z. Chen and B. Cockburn, *Analysis of a finite element method for the drift-diffusion semiconductor device equations: the multidimensional case*, Num. Math., **71**, 1–28 (1995).
- [6] P. Degond, F. Delaurens and F.J. Mustieles, *Semiconductor modelling via the Boltzmann equation*, Computing Methods in Applied Sciences and Engineering, SIAM, 311–324 (1990).
- [7] P. Degond, *Macroscopic limits of the Boltzmann equation: a review*, Modeling and computational methods for kinetic equations, Model. Simul. Sci. Eng. Technol., Birkhäuser Boston, 3–57 (2004).
- [8] E. Fatemi and F. Odeh, *Upwind finite difference solution of Boltzmann equation applied to electron transport in semiconductor devices*, J. Comput. Phys., **108**, 209–217 (1993).
- [9] M. Galler and F. Schürerer, *A deterministic solution method for the coupled system of transport equations for the electrons and phonons in polar semiconductors*, J. Phys. A, **37**, 1479–1497 (2004).
- [10] I.M. Gamba, *Behavior of the potential at the pn-Junction for a model in semiconductor theory*, Appl. Math. Lett., **3**, 59–63 (1990).
- [11] I.M. Gamba, *Asymptotic boundary conditions for an oxide region in a semiconductor device*, Asymptotic Anal., **7**, 37–48 (1993).
- [12] I.M. Gamba, *Asymptotic behavior at the boundary of a semiconductor device in two space dimensions*, Ann. Mat. Pura App. (IV), **CLXIII**, 43–91 (1993).
- [13] T. Gonzales and D. Pardo, *Physical models of ohmic contact for Monte Carlo device simulation*, Solid-State Electronics, **39**, No. 4, 555–562 (1996).
- [14] P. Grisvard, *Elliptic Problems in Non-smooth Domains*, Monographs and Studies in Mathematics, **24**, Pitman, London (1985).
- [15] C. Jacoboni and P. Lugli, *The Monte Carlo Method for Semiconductor Device Simulation*, Springer-Verlag, New York (1989).

- [16] J.W. Jerome and C.-W. Shu, *Energy models for one-carrier transport in semiconductor devices*, in IMA Volumes in Mathematics and Its Applications, Vol. 59, W. Coughran, J. Cole, P. Lloyd and J. White, editors, Springer-Verlag, 185–207 (1994).
- [17] G. Jiang and C.-W. Shu, *Efficient implementation of weighted ENO schemes*, J. Comput. Phys., **126**, 202–228 (1996).
- [18] A. Majorana, C. Milazzo and O. Muscato, *Charge transport in 1D silicon devices via Monte Carlo simulation and Boltzmann-Poisson solver*, COMPEL, **23**, 410–425 (2004).
- [19] A. Majorana and R.M. Pidotella, *A finite difference scheme solving the Boltzmann-Poisson system for semiconductor devices*, J. Comput. Phys., **174**, 649–668 (2001).
- [20] J.M. Mantas, J.A. Carrillo and A. Majorana, *Parallelization of WENO-Boltzmann schemes for kinetic descriptions of 2D semiconductor devices*, to appear in Mathematics for Industry Springer Series (2005).
- [21] P.A. Markowich, C. Ringhofer and C. Schmeiser, *Semiconductor Equations*, Springer-Verlag, New-York (1990).
- [22] S. Selberherr, *Analysis and Simulations of Semiconductor Devices*, Springer, Vienna (1984).
- [23] C.-W. Shu, *Essentially non-oscillatory and weighted essentially non-oscillatory schemes for hyperbolic conservation laws*, Lecture Notes in Mathematics **1697**, 325-432 (1998).
- [24] C.-W. Shu and S. Osher, *Efficient implementation of essentially non-oscillatory shock capturing schemes*, J. Comput. Phys., **77**, 439–471 (1988).
- [25] K. Tomizawa, *Numerical Simulation of Submicron Semiconductor Devices*, Artech House, Boston (1993).
- [26] W. Wagner, *Stochastic models and Monte Carlo algorithms for Boltzmann type equations*. Monte Carlo and quasi-Monte Carlo methods 2002, 129–153, Springer, Berlin (2004).

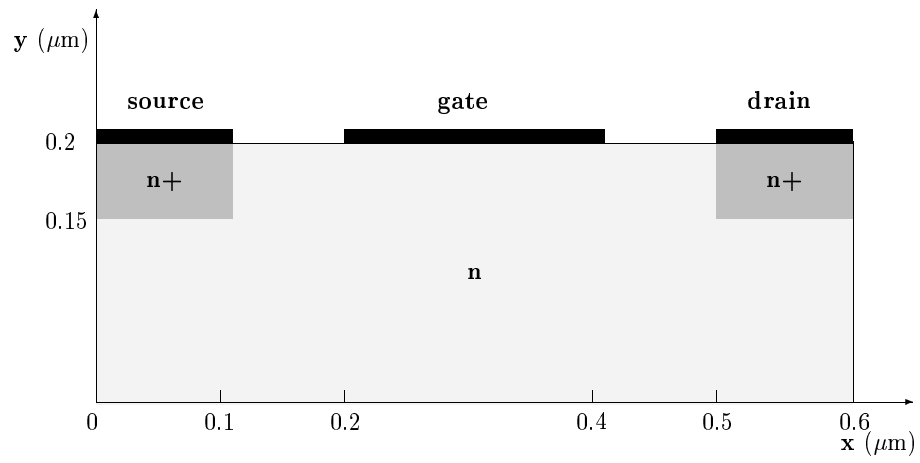


Figure 1: Schematic representation of a two dimensional MESFET.

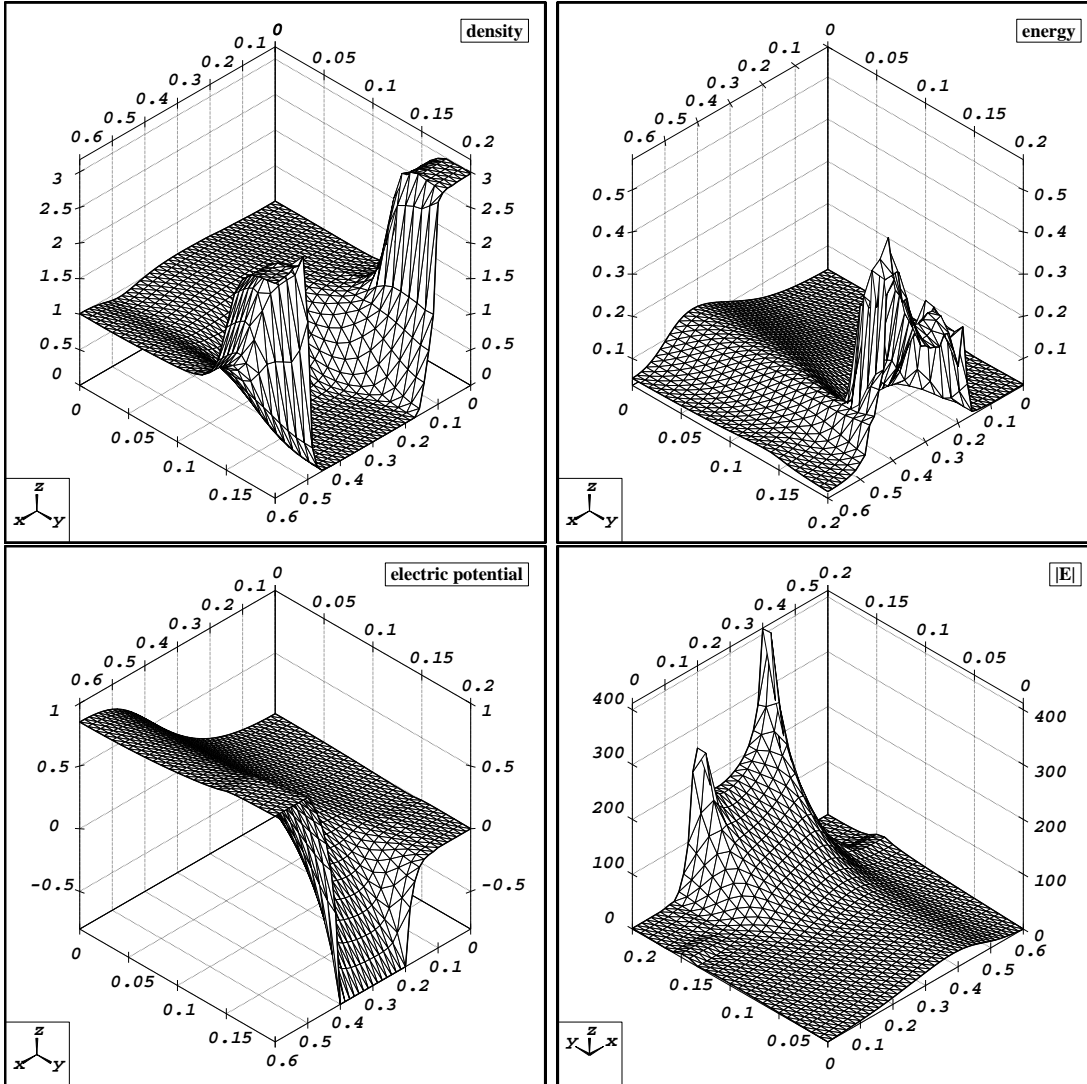


Figure 2: MESFET device. BTE results by grid A. $t = 5$ ps. Top left: the charge density ρ ($10^{-17} \cdot \text{cm}^{-3}$); top right: the energy \mathcal{E} (eV); bottom left: the electric potential V ; bottom right: $|\mathbf{E}|$ (kV/cm).

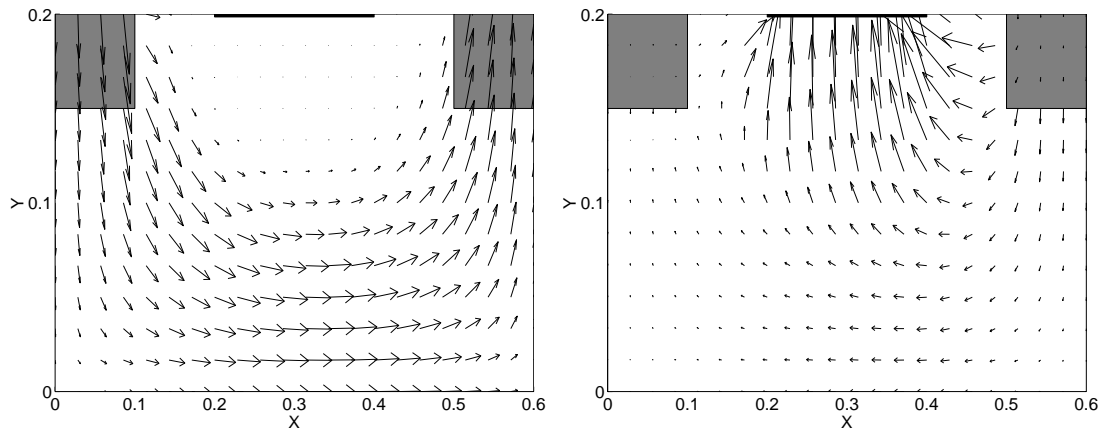


Figure 3: MESFET device. BTE results by grid A. $t = 5$ ps. Left: the current; right: the electric field \mathbf{E} .

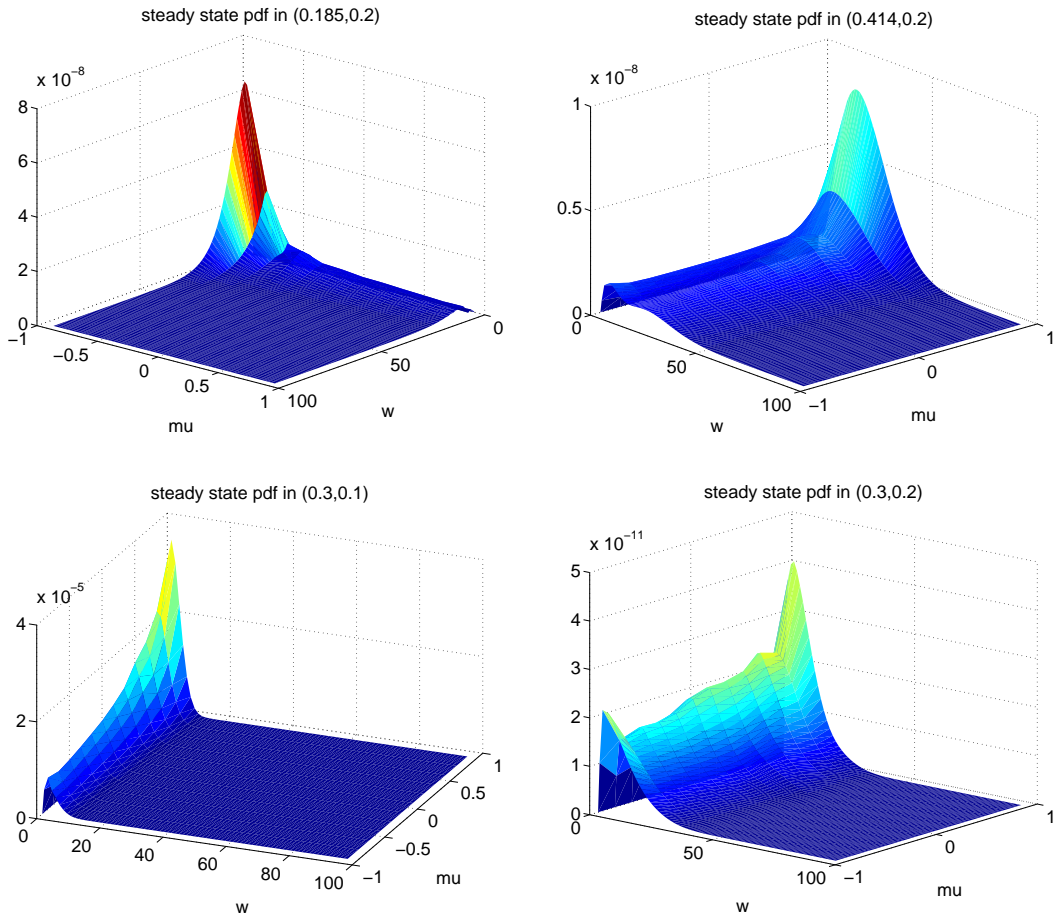


Figure 4: MESFET device. BTE results. $t = 5$ ps. Pdf's in steady state averaged over ϕ at different locations of the MESFET. Top left: at $(x, y) = (0.185, 0.2)$; top right: at $(x, y) = (0.414, 0.2)$; bottom left: at $(x, y) = (0.3, 0.1)$; bottom right: at $(x, y) = (0.3, 0.2)$.

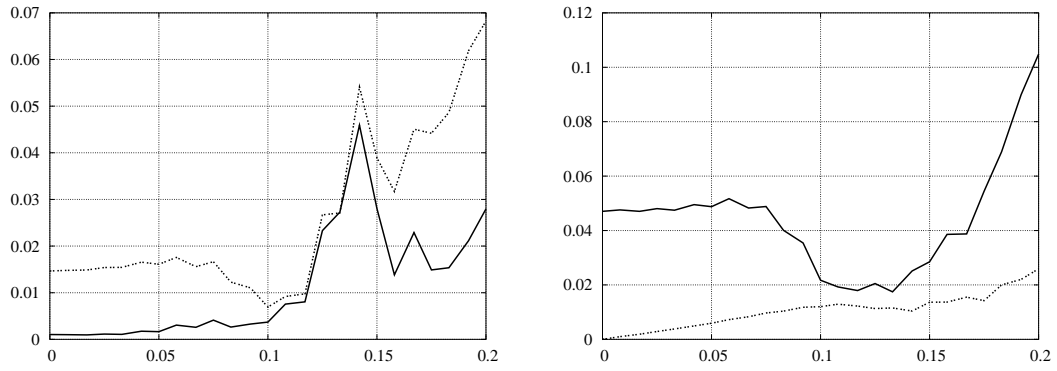


Figure 5: MESFET device. BTE results. $t = 5$ ps. Discrepancies (2.14) between the grids A-B as a function of y . Left: the density ρ (continuous line) and the total energy $\rho\mathcal{E}$ (dashed line); right: the x -momentum ρu_x (continuous line) and the y -momentum ρu_y (dashed line).

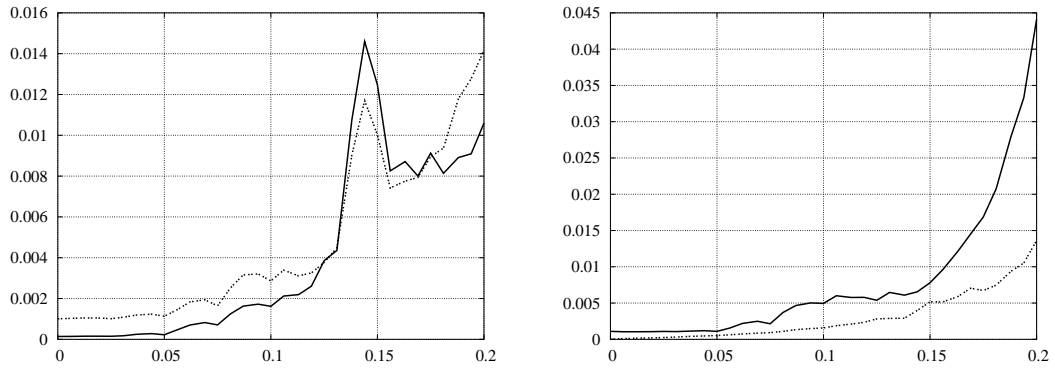


Figure 6: MESFET device. BTE results. $t = 5$ ps. Discrepancies (2.14) between the grids A-C as a function of y . Left: the density ρ (continuous line) and the total energy $\rho\mathcal{E}$ (dashed line); right: the x -momentum ρu_x (continuous line) and the y -momentum ρu_y (dashed line).

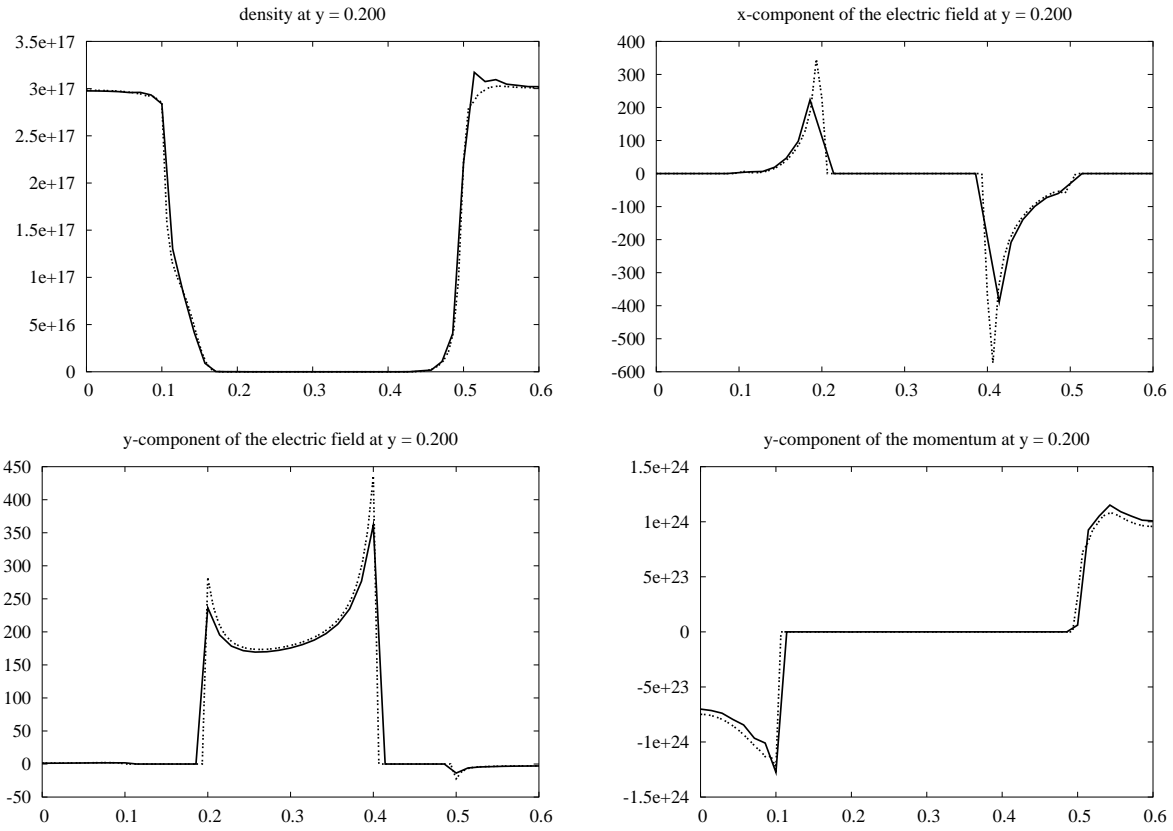


Figure 7: MESFET device. BTE results. $t = 5$ ps. Comparisons between different grids at $y = 0.2$. Solid line: grid A, dashed line: grid C. Top left: density ρ ; top right: x -component of the electric field \mathbf{E} ; bottom left: y -component of the electric field \mathbf{E} ; bottom right: the x -momentum ρu_x .

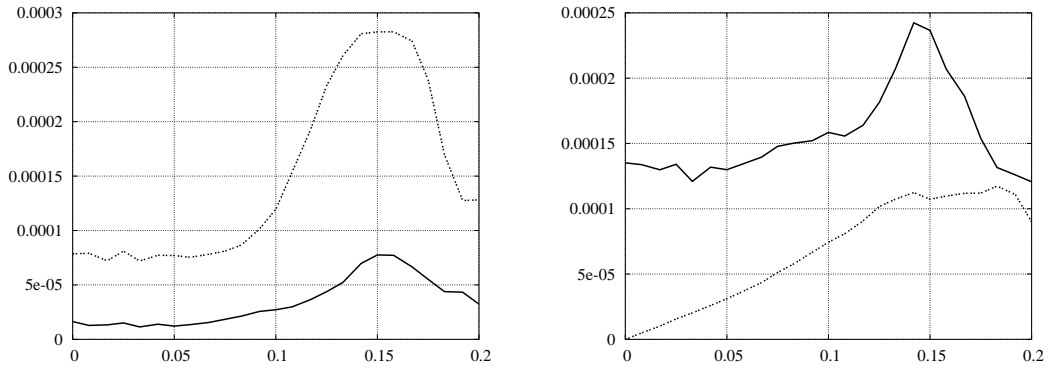


Figure 8: MESFET device. BTE results. $t = 5$ ps. Discrepancies (2.14) between the grids A- \mathbf{E}_{cut} as a function of y . Left: the density ρ (continuous line) and the total energy $\rho\mathcal{E}$ (dashed line); right: the x -momentum ρu_x (continuous line) and the y -momentum ρu_y (dashed line).

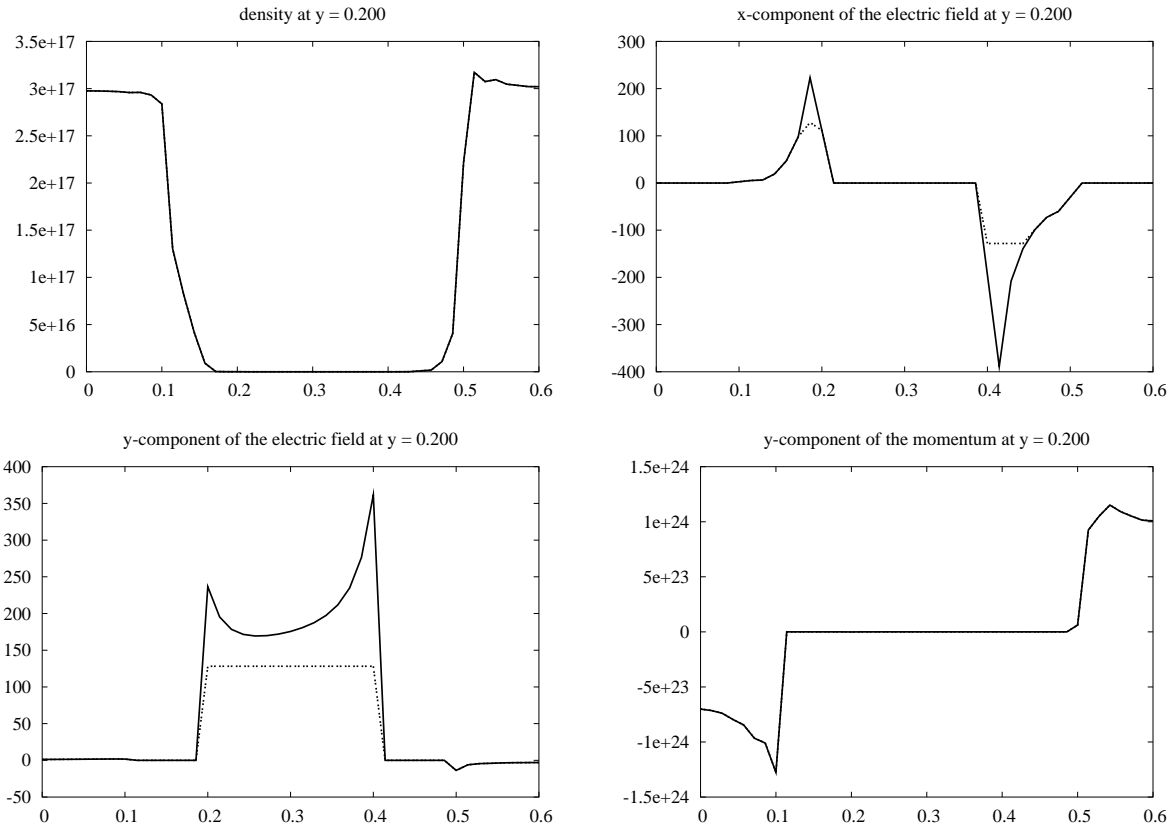


Figure 9: MESFET device. BTE results. $t = 5$ ps. Comparisons between different grids at $y = 0.2$. Solid line: grid A, dashed line: grid E_{cut} . Top left: density ρ ; top right: x -component of the electric field \mathbf{E} ; bottom left: y -component of the electric field \mathbf{E} ; bottom right: the x -momentum ρu_x .

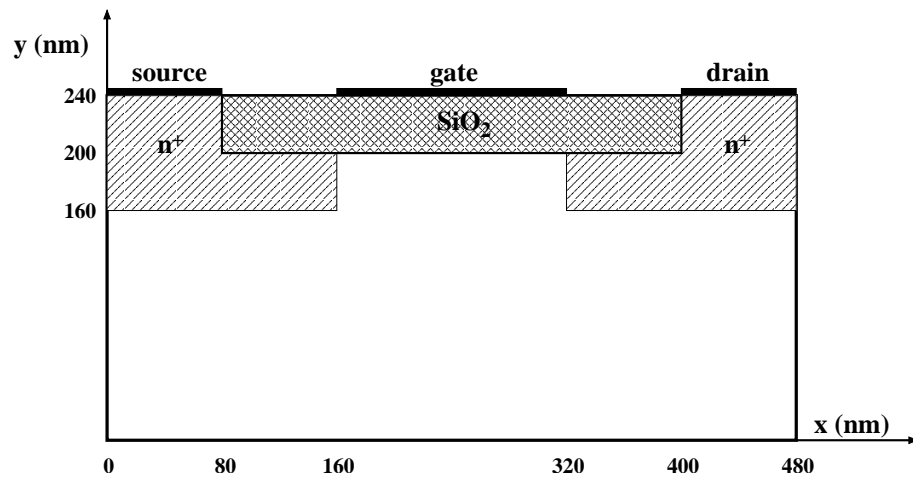


Figure 10: Schematic representation of a two dimensional MOSFET.

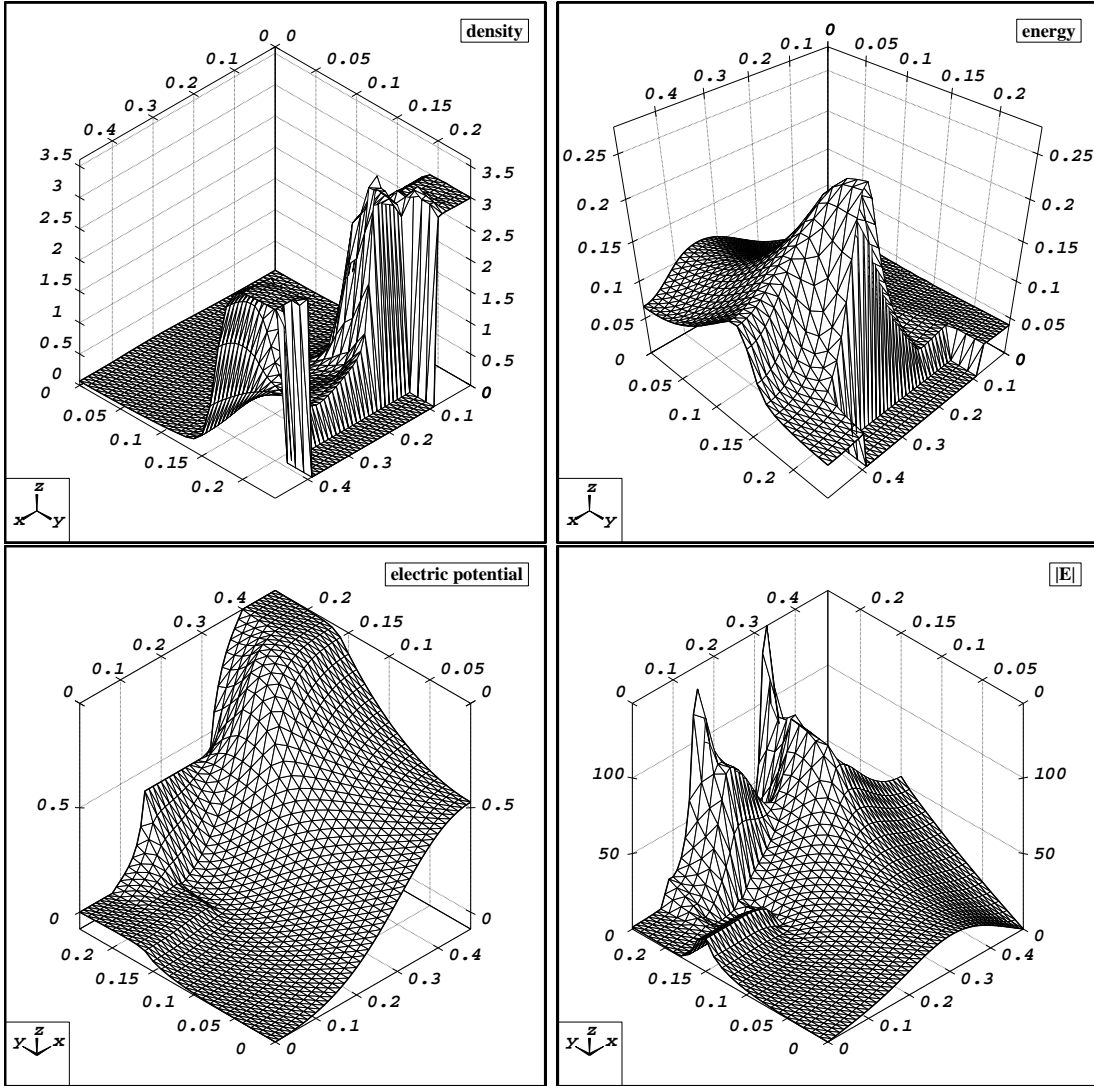


Figure 11: MOSFET device. BTE results. $t = 5$ ps. Top left: the charge density ρ ($10^{-17} \cdot \text{cm}^{-3}$); top right: the energy \mathcal{E} (eV); bottom left: the electric potential V ; bottom right: $|\mathbf{E}|$ (kV/cm).

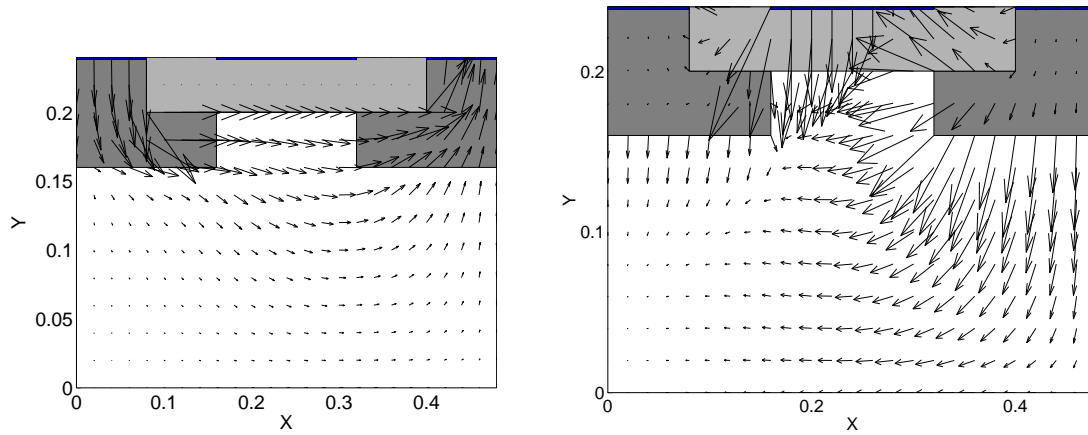


Figure 12: MOSFET device. BTE results. $t = 5$ ps. Left: the current; right: the electric field \mathbf{E} .

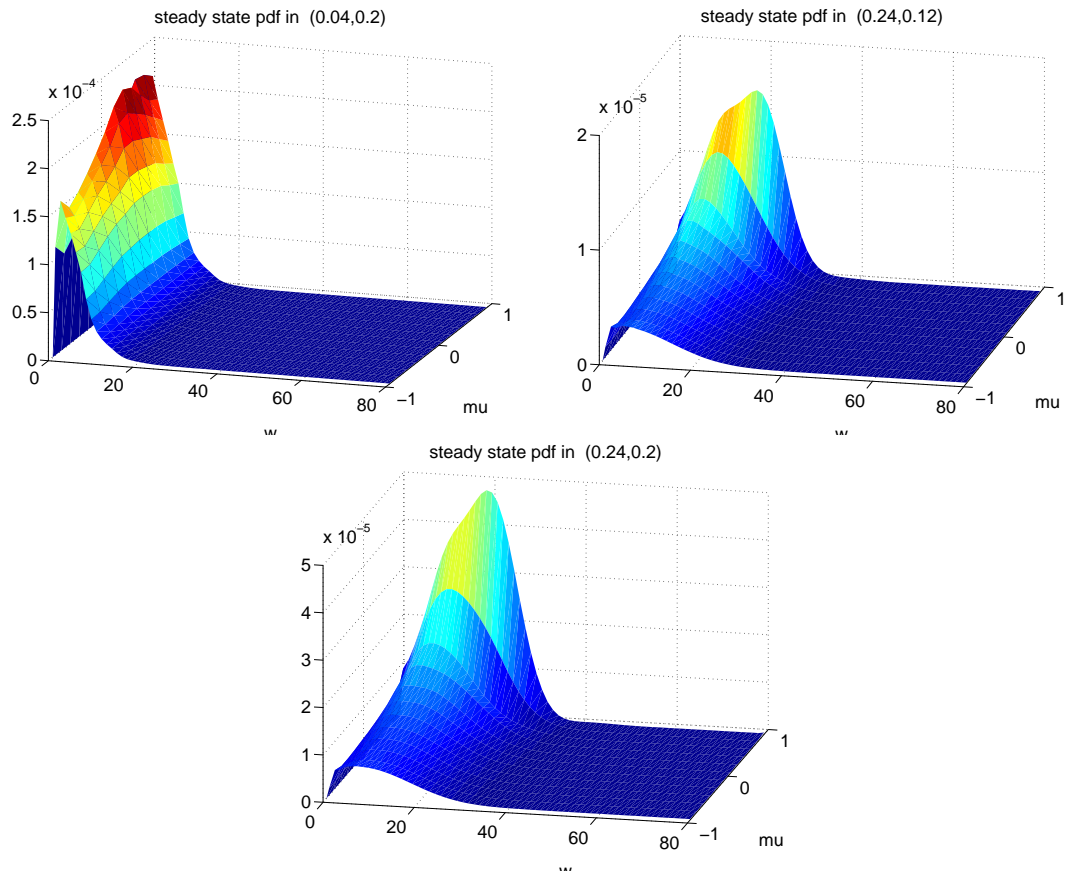


Figure 13: MOSFET device. BTE results. $t = 5$ ps. Pdf's in steady state averaged over ϕ at different locations of the MOSFET. Top left: at $(x, y) = (0.04, 0.2)$; top right: at $(x, y) = (0.24, 0.12)$; bottom: at $(x, y) = (0.24, 0.2)$.

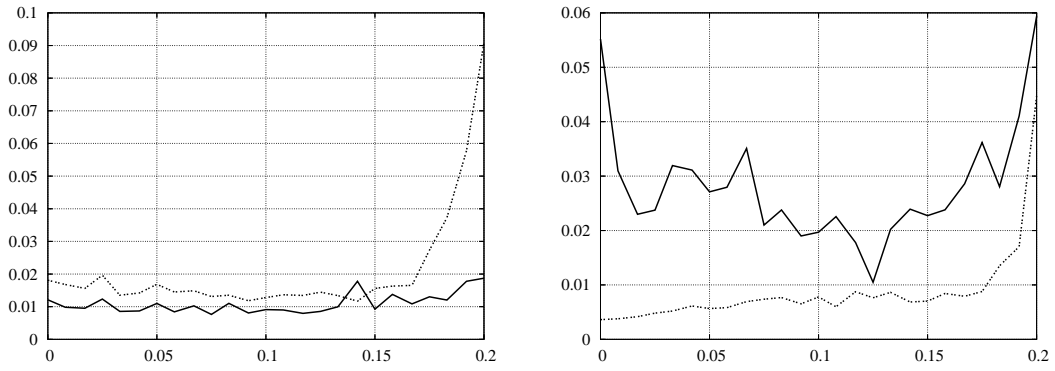


Figure 14: MESFET device. $t = 5$ ps. Discrepancies (2.14) between the BTE result (grid A) and the DSMC result as a function of y . Left: the density ρ (continuous line) and the total energy $\rho\mathcal{E}$ (dashed line); right: the x -momentum ρu_x (continuous line) and the y -momentum ρu_y (dashed line).

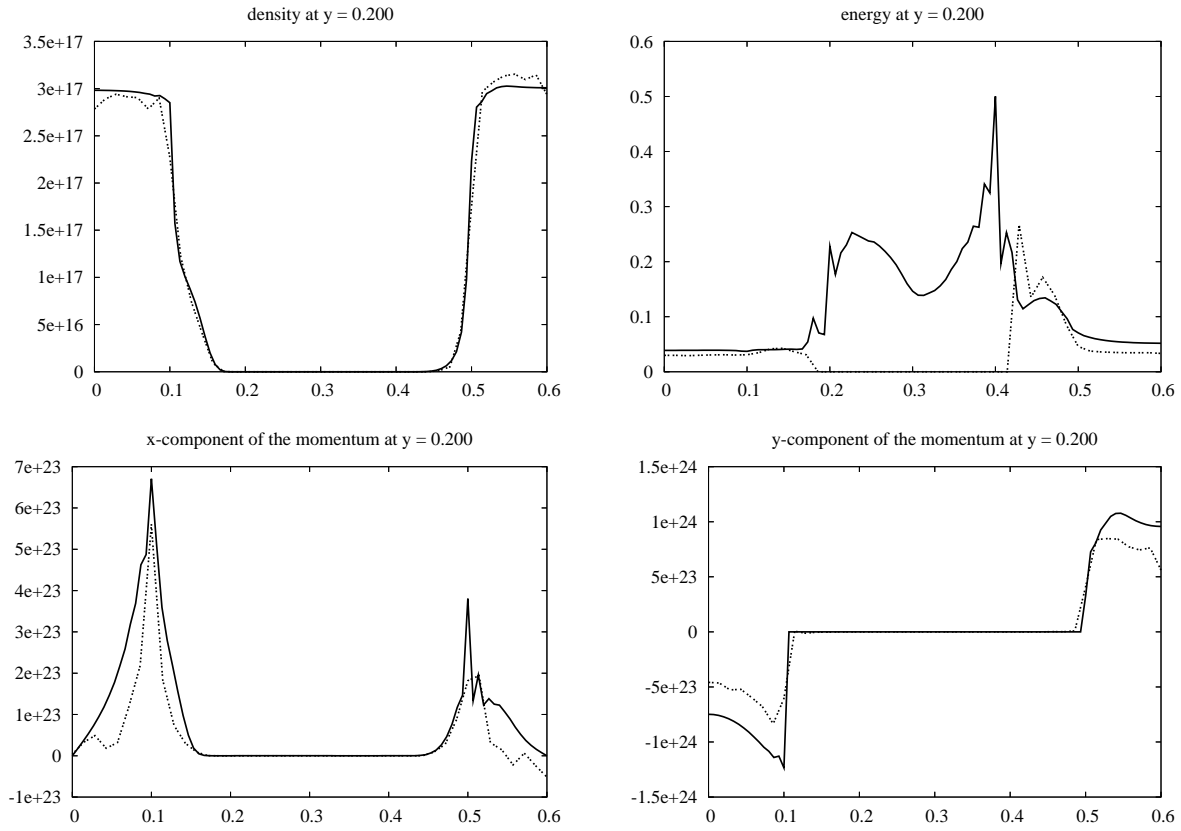


Figure 15: MESFET device. Comparisons between the BTE and the DSMC results at $t = 5$ ps and $y = 0.2$. Solid line: the BTE results (grid C), dashed line: the DSMC results. Top left: density ρ ; top right: energy \mathcal{E} ; bottom left: the x -momentum ρu_x ; bottom right: the y -momentum ρu_y .

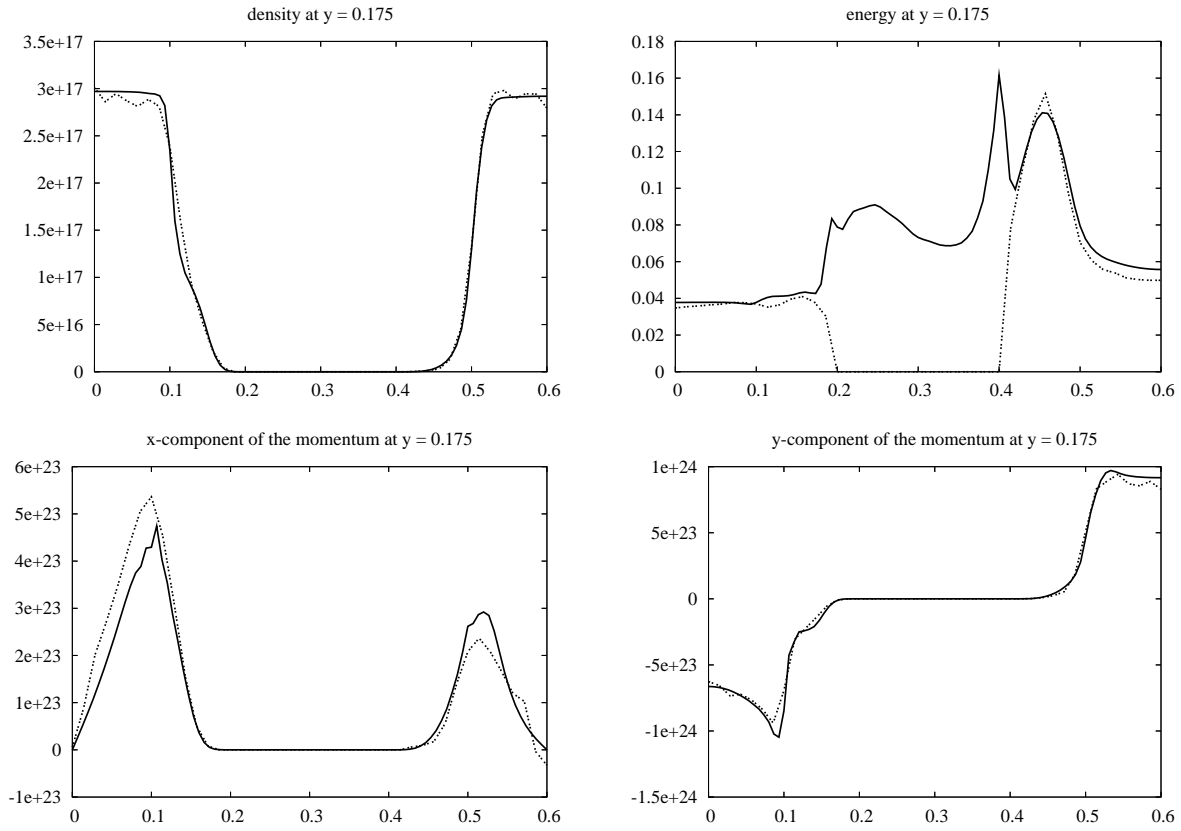


Figure 16: MESFET device. Comparisons between the BTE and the DSMC results at $t = 5$ ps and $y = 0.175$. Solid line: the BTE results (grid C), dashed line: the DSMC results. Top left: density ρ ; top right: energy \mathcal{E} ; bottom left: the x -momentum ρu_x ; bottom right: the y -momentum ρu_y .

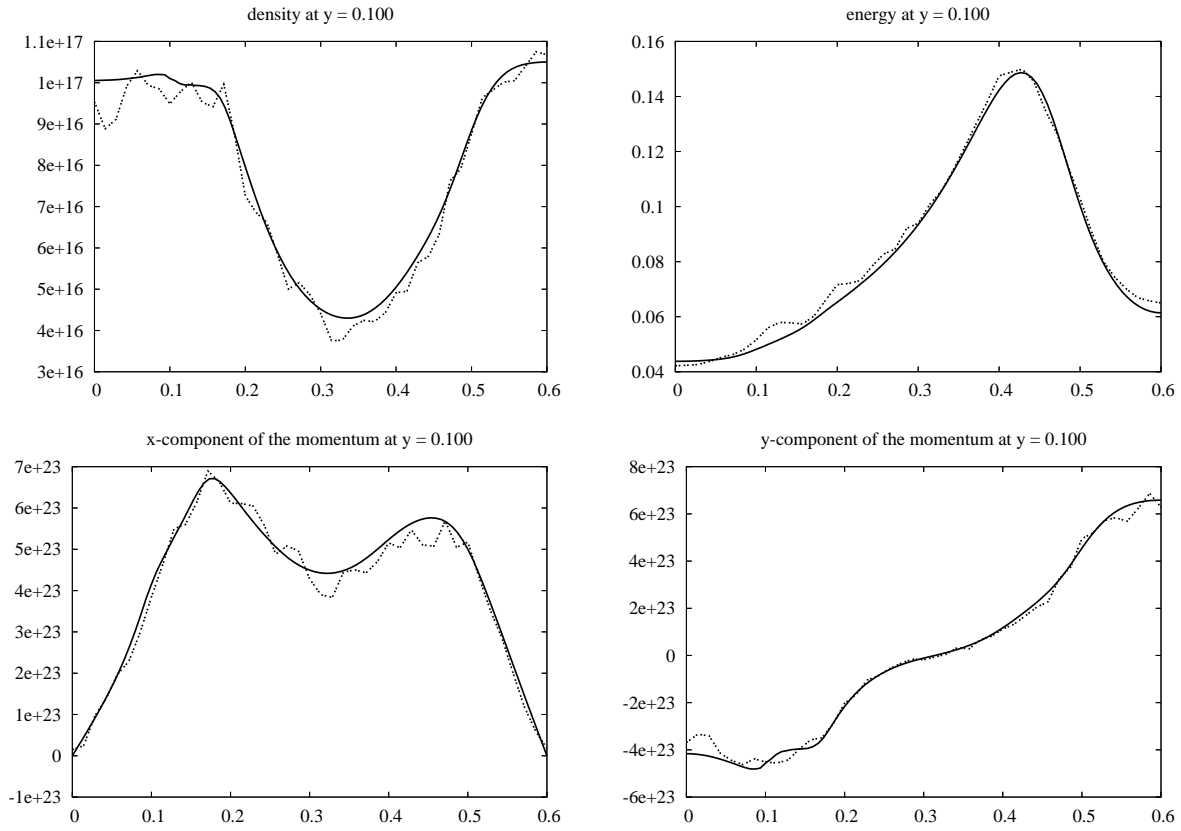


Figure 17: MESFET device. Comparisons between the BTE and the DSMC results at $t = 5$ ps and $y = 0.1$. Solid line: the BTE results (grid C), dashed line: the DSMC results. Top left: density ρ ; top right: energy \mathcal{E} ; bottom left: the x -momentum ρu_x ; bottom right: the y -momentum ρu_y .

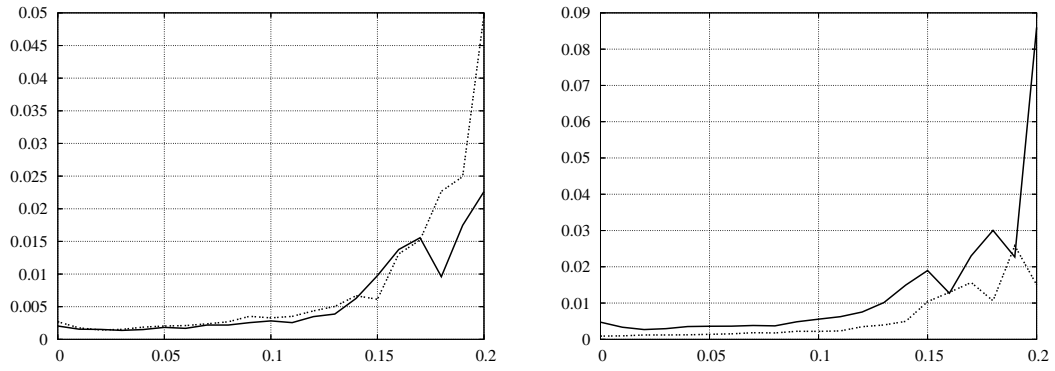


Figure 18: MOSFET device. $t = 5$ ps. Discrepancies (2.14) between the BTE and the DSMC results as a function of y . Left: the density ρ (continuous line) and the total energy $\rho\mathcal{E}$ (dashed line); right: the x -momentum ρu_x (continuous line) and the y -momentum ρu_y (dashed line).

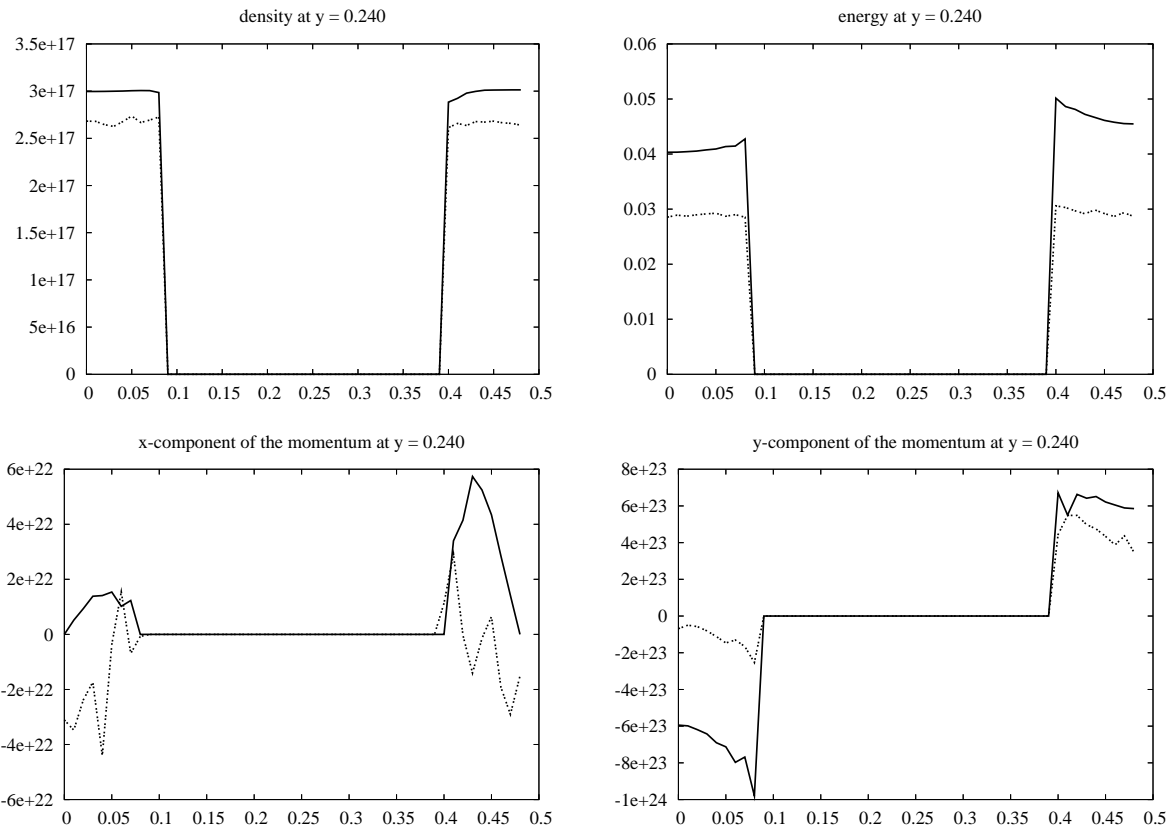


Figure 19: MOSFET device. Comparisons between the BTE and the DSMC results at $t = 5$ ps and $y = 0.24$. Solid line: the BTE results, dashed line: the DSMC results. Top left: density ρ ; top right: energy \mathcal{E} ; bottom left: the x -momentum ρu_x ; bottom right: the y -momentum ρu_y .

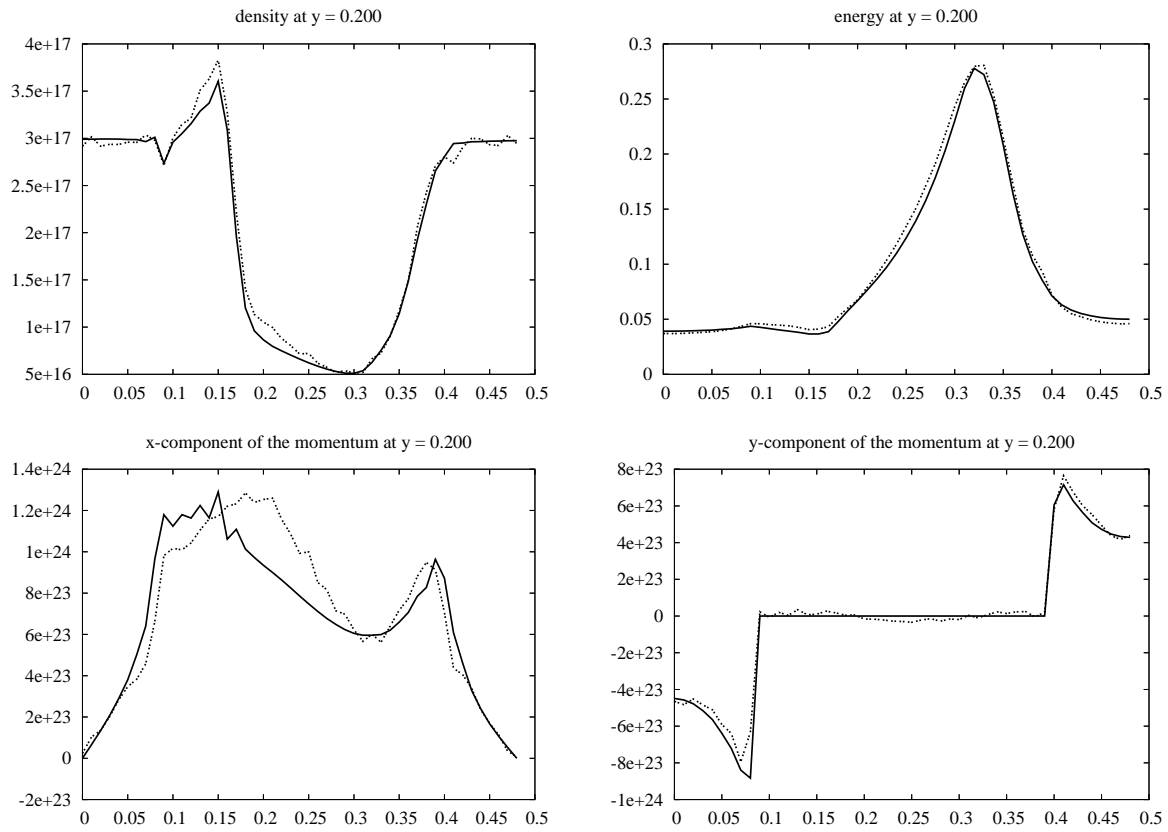


Figure 20: MOSFET device. Comparisons between the BTE and the DSMC results at $t = 5$ ps and $y = 0.12$. Solid line: the BTE results, dashed line: the DSMC results. Top left: density ρ ; top right: energy \mathcal{E} ; bottom left: the x -momentum ρu_x ; bottom right: the y -momentum ρu_y .

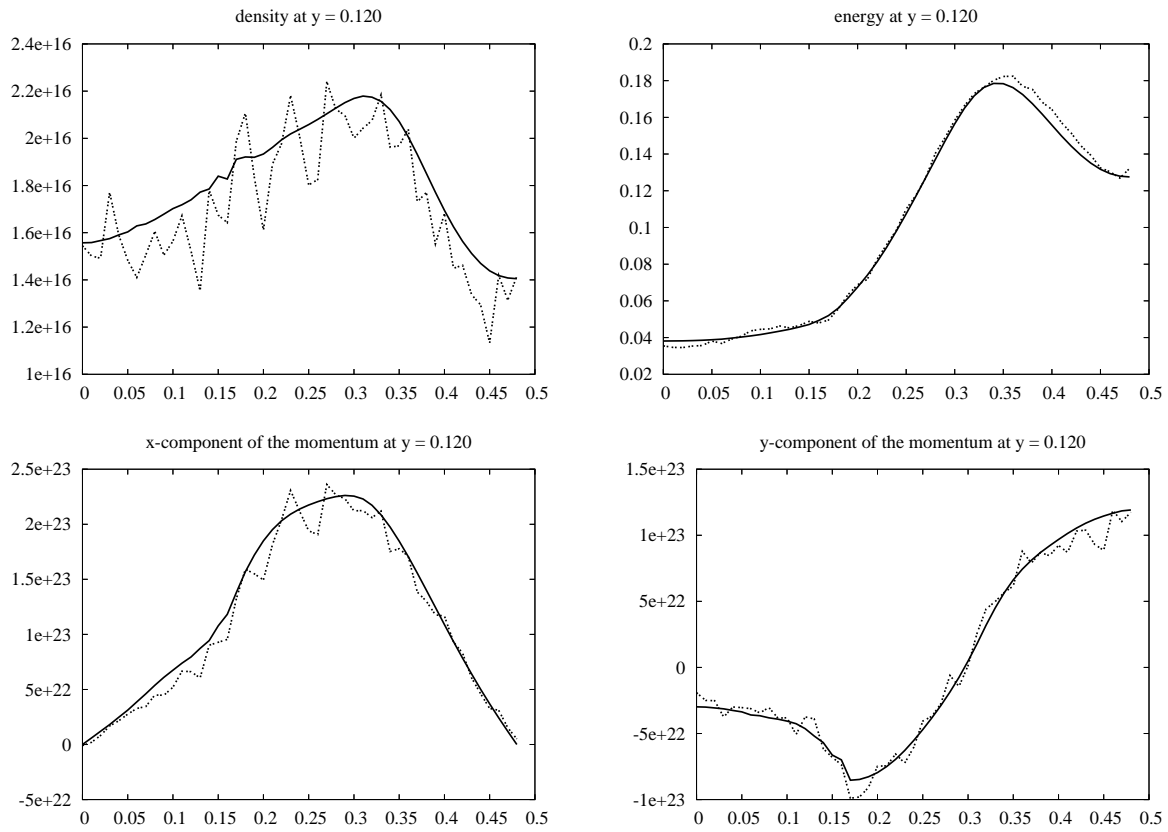


Figure 21: MOSFET device. Comparisons between the BTE and the DSMC results at $t = 5$ ps and $y = 0.12$. Solid line: the BTE results, dashed line: the DSMC results. Top left: density ρ ; top right: energy \mathcal{E} ; bottom left: the x -momentum ρu_x ; bottom right: the y -momentum ρu_y .